



A New Sample of Warm Extreme Debris Disks from the ALLWISE Catalog

Attila Moór^{1,2}, Péter Ábrahám^{1,2}, Gyula Szabó^{3,4}, Krisztián Vida^{1,2}, Gianni Cataldi^{5,6}, Alíz Derekas^{3,4}, Thomas Henning⁷, Karen Kinemuchi⁸, Ágnes Kóspál^{1,2,7}, József Kovács^{3,4}, András Pál^{1,2}, Paula Sarkis⁷, Bálint Seli^{1,9}, Zsófia M. Szabó^{1,9}, and Katalin Takáts¹⁰

¹ Konkoly Observatory, Research Centre for Astronomy and Earth Sciences, Eötvös Loránd Research Network (ELKH) Konkoly-Thege Miklós út 15-17, 1121 Budapest, Hungary; moor@konkoly.hu

² ELTE Eötvös Loránd University, Institute of Physics, Pázmány Péter sétány 1/A, 1117 Budapest, Hungary

³ ELTE Eötvös Loránd University, Gothard Astrophysical Observatory, Szombathely, Hungary

⁴ MTA-ELTE Exoplanet Research Group, 9700 Szombathely, Szent Imre h.u. 112, Hungary

⁵ National Astronomical Observatory of Japan, Osawa 2-21-1, Mitaka, Tokyo 181-8588, Japan

⁶ Department of Astronomy, Graduate School of Science, The University of Tokyo, 7-3-1 Hongo, Bunkyo-ku, Tokyo 113-0033, Japan

⁷ Max-Planck-Institut für Astronomie, Königstuhl 17, D-69117 Heidelberg, Germany

⁸ Apache Point Observatory and New Mexico State University, Sunspot, NM 88349, USA

⁹ Eötvös Loránd University, Department of Astronomy, Pázmány Péter sétány 1/A, 1117 Budapest, Hungary

¹⁰ Departamento de Ciencias Físicas, Universidad Andrés Bello, Avda. República 252, 32349 Santiago, Chile

Received 2020 October 14; revised 2021 January 12; accepted 2021 January 13; published 2021 March 23

Abstract

Extreme debris disks (EDDs) are rare systems with peculiarly large amounts of warm dust that may stem from recent giant impacts between planetary embryos during the final phases of terrestrial planet growth. Here we report on the identification and characterization of six new EDDs. These disks surround F5-G9 type main-sequence stars with ages >100 Myr, have dust temperatures higher than 300 K, and fractional luminosities between 0.01 and 0.07. Using time-domain photometric data at 3.4 and 4.6 μm from the WISE all-sky surveys, we conclude that four of these disks exhibited variable mid-infrared (IR) emission between 2010 and 2019. Analyzing the sample of all known EDDs, now expanded to 17 objects, we find that 14 of them showed changes at 3–5 μm over the past decade, suggesting that mid-IR variability is an inherent characteristic of EDDs. We also report that wide-orbit pairs are significantly more common in EDD systems than in the normal stellar population. While current models of rocky planet formation predict that the majority of giant collisions occur in the first 100 Myr, we find that the sample of EDDs is dominated by systems older than this age. This raises the possibility that the era of giant impacts may be longer than we think, or that some other mechanism(s) can also produce EDDs. We examine a scenario where the observed warm dust stems from the disruption and/or collisions of comets delivered from an outer reservoir into the inner regions, and explore what role the wide companions could play in this process.

Unified Astronomy Thesaurus concepts: Circumstellar disks (235); Debris disks (363); Exozodiacal dust (500); Extrasolar rocky planets (511); Infrared excess (788); Time domain astronomy (2109)

1. Introduction

Debris disks comprise planetesimals and their erosional products down to micrometer-sized dust particles (Wyatt 2008; Krivov 2010). From this mixture of solids of different sizes, only the smallest particles are observable. The majority of debris disks have been detected based on the infrared (IR) excess caused by thermal emission from their optically thin dust material. Large far-IR surveys with the Spitzer Space Telescope (Spitzer; Werner et al. 2004) and the Herschel Space Observatory (Pilbratt et al. 2010) indicated that at least 20% of main-sequence A–K-type stars are encircled by cold dust ($\lesssim 100$ K), implying the presence of debris belts at tens of astronomical units from the central stars (Su et al. 2006; Thureau et al. 2014; Montesinos et al. 2016; Hughes et al. 2018; Sibthorpe et al. 2018). These structures are analogous to the Kuiper Belt of our solar system. Their dust particles, which are continuously removed by interactions with the radiation forces of the star and/or with the stellar wind, are thought to be replenished by a collisional cascade involving larger bodies.

Analysis of the spectral energy distribution (SED) implies that a fraction of systems with cold debris dust also host warmer (>150 K) dust particles, suggesting that an inner debris ring resembling our asteroid belt also exists around the star (Chen et al. 2014; Kennedy & Wyatt 2014; Ertel et al. 2020).

We also know of some systems that possess only warm dust (e.g., Beichman et al. 2011). The majority of these warm dust belts can be explained as a product of long-term collisional evolution of a planetesimal belt colocated with the dust (Geiler & Krivov 2017). Alternatively, or in addition to the in situ dust generation, disrupting comets delivered from an outer reservoir (Nesvorný et al. 2010; Bonsor et al. 2012) or grains transported inward from an outer debris cloud under the influence of Poynting–Robertson and stellar wind drag (Reidemeister et al. 2011; Kennedy & Piette 2015; Rigley & Wyatt 2020) can also produce warm dust particles in the inner regions.

The last 15 yr have seen the discovery of several FGK-type main-sequence stars that host unusually dust-rich warm debris disks with typical dust temperature of >300 K and with fractional luminosity ($f_d = L_{\text{disk}}/L_*$) of >0.01 . These fractional luminosities are three orders of magnitude higher than those of typical warm debris systems, and suggest that these *extreme debris disks* (EDDs; Balog et al. 2009) are at least partly optically thick for the stellar illumination. EDDs share some additional common properties. Mid-IR spectroscopic observations revealed that they tend to show strong solid-state emission features, implying the presence of small, submicron-sized crystalline dust particles (Rhee et al. 2008; Olofsson et al. 2012; Lisse et al. 2020). Even more uniquely, their photometric

monitoring with Spitzer demonstrated that most EDDs display significant variability on monthly to yearly timescales at 3–5 μm (Meng et al. 2014, 2015; Su et al. 2019b). The ages of known EDDs fall predominantly in the range between 10 and 200 Myr; the only exception is BD+20 307 with an age of >1 Gyr (Weinberger et al. 2011).

The peculiarly high dust content of EDDs is orders of magnitude above what can be explained by a steady-state grinding down process of an in situ planetesimal population that started when the system was formed (e.g., Wyatt et al. 2007). Instead, the observed properties point to a recent, episodic increase in dust production, which may be related to a giant collision of planetary embryos in the inner 1–2 au region (Melis et al. 2010; Su et al. 2019b). Similar collisions—including the Moon-forming event between the proto-Earth and a planetary embryo—are thought to be common during the final accumulation of terrestrial planets in the early ($\lesssim 100$ Myr) solar system (Chambers 2013). Such impacts produce a large quantity of debris material that escapes the planets entirely, forming a dust disk that causes significant mid-IR excess for a period (Jackson & Wyatt 2012; Genda et al. 2015). In this scenario, the observed rapid time variations can be linked to the orbital and collisional evolution of the dust and vapor cloud that emerged from the impact event (Su et al. 2019b). Submicron-sized grains produced in optically thick clumps of vapor condensates can explain the observed prominent 10 μm solid-state features (Su et al. 2020).

By studying EDDs, we can learn more about the immediate aftermath of major transient dust production events possibly associated to giant impacts. Such investigations thus also have the potential to improve our knowledge on the formation of terrestrial planets. However, EDDs are rare objects; currently only 11¹¹ such disks are known (Appendix C). To understand this phenomenon in greater detail, we need a larger sample. In the present work, we aim to identify additional EDDs around sunlike stars and study their properties with special regard to IR variability and age distribution. The discovery of currently known EDDs in the literature was mainly based on IR data from the Infrared Astronomical Satellite (IRAS; Neugebauer et al. 1984) survey and from dedicated Spitzer programs targeting young open clusters. In our study we use photometry obtained with the Wide-field Infrared Survey Explorer (WISE; Wright et al. 2010), which scanned the whole sky in four IR bands, at 3.4 μm (W1), 4.6 μm (W2), 12 μm (W3), and 22 μm (W4). Thanks to its substantially better sensitivity in the latter two bands than IRAS had at 12 and 25 μm , WISE offers an excellent opportunity to search for warm debris disks over the entire sky, as has already been demonstrated by several studies (e.g., Kennedy & Wyatt 2013; Cruz-Saenz de Miera et al. 2014; Patel et al. 2014, 2017; Cotten & Song 2016). The two shorter-wavelength bands enable the detection and characterization of hot dust at temperatures above 400 K. The WISE satellite is still in operation and has been continuing the all-sky surveys at 3.4 and 4.6 μm , providing photometry spaced by 6 months. Our study on IR variability of EDDs is principally based on this data set.

¹¹ This number refers only to EDDs hosted by FGK-type main-sequence stars. We note that recent years have seen the discovery of several young M dwarf stars with warm circumstellar disks having extremely high fractional luminosity (Flaherty et al. 2019; Zuckerman et al. 2019; Silverberg et al. 2020). These systems may have a mixed nature; while some of them are probably long-lived accretion disks (e.g., Silverberg et al. 2020), some may harbor debris disks (Zuckerman et al. 2019).

This paper is structured as follows. Section 2 reviews our investigation to search for new EDD systems utilizing the AllWISE IR (Cutri et al. 2013) and the Tycho-Gaia Astrometric Solution (TGAS; Michalik et al. 2015; Lindegren et al. 2016) astrometric catalogs. Our procedure—in which we took special care to filter out possible false disk identifications—resulted in six disks. In Section 3 we discuss the characterization of the host stars including the age estimates of the systems. The determination of the disk properties is described in Section 4, while the mid-IR variability of the selected objects is studied in Section 5. We then discuss our results (Section 6) and provide a summary of the work (Section 7).

2. Identification of New EDDs

Aimed at revealing new EDDs hosted by sunlike (F5-K7-type) stars, we took mid-IR photometric data from the AllWISE catalog and combined them with astrometric information from the TGAS database. The AllWISE data release is based on observations from the WISE cryogenic and NEOWISE post-cryogenic survey phases of the WISE mission obtained in 2010–2011. The catalog contains positions and four-band (W1–W4) mid-IR photometric information for ~ 750 million sources. To reduce the chance of source confusion and contamination from strong diffuse background emission, we discarded all sources located within 5° of the Galactic plane. Correspondingly to our targeted spectral type range, we selected objects with $J - K_s$ color index between 0.22 and 0.8. The conversion between spectral types and colors was adopted from Pecaut & Mamajek (2013). To discard suspicious WISE photometric data from the compiled sample, we applied a number of additional selection criteria. We only used sources where, (1) the W1, W2, and W3 band flux measurements have signal-to-noise ratios (S/Ns) > 10 ; (2) the W4 band measurement has a S/N of > 3 ; and (3) the reduced χ^2 ($w1rchi2-w4rchi2$) of the profile-fit photometry measurement is < 3 in each band. Moreover, we removed all objects with contamination and confusion flags (`cc_flags`) of either “D,” “P,” “H,” or “O” in any of the four bands, i.e., where the photometry is probably affected by diffraction, persistence, halo, or ghost artifacts. In the finally selected sample, we corrected the potential overestimate of the real flux in saturated W2 photometry at 4.6 μm by applying the formula proposed by Cotten & Song (2016, Equation (5)).

The TGAS catalog provides a 5D astrometric solution for over 2 million sources. From this data set, we retained only those objects that are located within 300 pc of the Sun, and have a good-quality parallax measurement with $\pi/\sigma_\pi > 5$. We also eliminated giant stars from the list by removing TGAS sources with J -band absolute magnitude $M_J < 5 \times (J - K_s)$. We took near-IR photometry from the Two Micron All-Sky Survey (2MASS; Skrutskie et al. 2006). The applied criteria were developed based on Rhee et al. (2007), who used B - and V -band data, but—due to possible reddening—we based our formula on near-IR photometry, which is less sensitive to extinction.

Accounting for the epoch difference between the TGAS (J2015.0) and AllWISE (J2010.0) catalogs, we corrected the positions of the selected TGAS objects for proper motion. After applying all of the above selection criteria, we cross-matched the two samples adopting a match radius of $0''.3$. This resulted in a combined data set including 78,650 objects.

To identify new EDDs, we looked for objects exhibiting significant excess emission in the W2 and W3 bands. The W2 band excess was requested because we aim at examining the

mid-IR variability of the revealed disks. To assess possible excesses in both bands, we compared the measured $K_s - W2$ and $K_s - W3$ color indices with the predicted ones. The predicted $K_s - W2$ and $K_s - W3$ ($P_{K_s - W_i}$, where i is 2 or 3) values were inferred from the $J - K_s$ color of the stars using color-color sequences quoted in Table 5 of Pecaut & Mamajek (2013). The uncertainty of this prediction ($\sigma_{P_{K_s - W_i}}$) is estimated to be 2%. The significance of the excesses was then computed as

$$\chi_{E(K_s - W_i)} = \frac{E(K_s - W_i)}{\sigma_{E(K_s - W_i)}} = \frac{K_s - W_i - P_{K_s - W_i}}{\sigma_{E(K_s - W_i)}}, \quad (1)$$

where $\sigma_{E(K_s - W_i)}$ is the quadratic sum of the measured uncertainties in the K_s and W_i bands, and $\sigma_{P_{K_s - W_i}}$, i.e., $\sigma_{E(K_s - W_i)} = \sqrt{\sigma_{K_s}^2 + \sigma_{W_i}^2 + \sigma_{P_{K_s - W_i}}^2}$. We selected those objects as EDD candidates where both $\chi_{E(K_s - W_2)}$ and $\chi_{E(K_s - W_3)}$ were higher than 5. This left us with 27 objects.

Looking at the candidates, we found that two of them were previously known EDDs (HD 23514 and BD+20 307). For a further 10 stars, the spectral type found in the literature does not correspond to the interval we selected. Four among them have A0–F2 spectral type, while the other six objects are nearby M-type stars. By comparing with the proper atmospheric models, the latter six no longer show significant excess. For 10 objects, the SED based on W1–W4 data is parallel to the stellar photosphere defined by the 2MASS measurements, but at a higher absolute level. Based on the literature, all of these objects are eclipsing binaries. According to the AllWISE catalog, six of them were probably variable in the W2 band as indicated by the value of their variability flag (`var_flag`), which has been set to the highest possible value of 9. Four of these objects probably displayed substantial changes in the W3 band, too. For these 10 binaries, our predicted photospheric colors ($P_{K_s - W_2}$, $P_{K_s - W_3}$) are probably inaccurate, and our excess detection is false. We note that two of these objects were already removed from our list because they have a spectral type that is too early. The WISE photometry of CD–48 8486, a G-type member of the Upper Centaurus Lupus group (Mamajek et al. 2002), also indicates an SED shifted upward with respect to the 2MASS near-IR data, suggesting that the excess identification is dubious. Earlier mid-IR photometric and spectroscopic observations of this source with Spitzer confirm this suspicion: the object shows no significant excess at wavelengths $< 25 \mu\text{m}$ (Silverstone et al. 2006; Carpenter et al. 2009).

The literature lists 11 EDDs with F–K-type host stars (Appendix C). Out of this sample, we recovered two objects, HD 23514 and BD+20 307. The other nine objects were excluded by our searching algorithm due to various reasons. HD 15407 and HD 166191 lie too close to the Galactic plane ($|b| < 5^\circ$), while RZ Psc, V488 Per, HD 113766, ID 8, and P 1121 are not included in the TGAS catalog. HD 145263 has an earlier spectral type than the other targets; its $J - K_s$ color index is outside our specified range. The disk of TYC 8241 2652 1 had been substantially depleted before the start of the WISE mission (Appendix C) and no longer exhibited strong excess in the W2 and W3 bands.

The detailed analysis, described above, left us with six EDD candidates out of the 27 initially selected sources. They are: TYC 4515-485-1 (hereafter TYC 4515), TYC 5940-1510-1

(TYC 5940), TYC 8105-370-1 (TYC 8105), TYC 4946-1106-1 (TYC 4946), TYC 4209-1322-1 (TYC 4209), and TYC 4479-3-1 (TYC 4479). However, due to the large WISE beam source, confusion or contamination by extended emission cannot be ruled out even in these cases. In order to test this, we performed several additional checks, but based on the currently available IR data, we found no sign of confusion or significant contamination at any of the selected systems (Appendix A). Therefore, throughout the following analysis, we will assume that the excesses in all six cases come from warm circumstellar dust disks. Previously, one of these objects, TYC 4479, was identified as a debris disk system (Cotten & Song 2016), while the other five disks are new discoveries.

Figure 1 shows the vicinity of the six systems in all four WISE bands (using the “unWISE” coadds, see Appendix A), while Table 1 summarizes astrometric and photometric data of the host stars. Although, during the selection process, we used TGAS astrometry, in this table we list more precise astrometric parameters taken from the Gaia EDR3 catalog (Gaia Collaboration et al. 2020; Lindegren et al. 2020).

3. Characterization of the Host Stars

3.1. Spectroscopic Observations

In order to estimate the fundamental parameters of the host stars of the identified EDDs, we performed high-resolution optical spectroscopy for all of them. As the observation log (Table 2) shows, we used four different high-resolution échelle spectrographs to obtain the spectra. One of our targets, TYC 4946, was measured twice.

TYC 5940, TYC 8105, and TYC 4946 were targeted with the Fiber-fed Extended Range Optical Spectrograph (FEROS; Kaufer et al. 1999) on the MPG/ESO 2.2 m (La Silla, Chile) telescope. This instrument has a mean spectral resolution of 48,000, covering the spectral region between 3500 and 9200 Å. In our observations, the object-sky operation mode was used, i.e., one of the two fibers was positioned at the star while the other was positioned at the sky. Reduction of FEROS spectra—including bias subtraction, flat-field correction, background subtraction, the definition and extraction of orders, and wavelength calibration—were performed using the FEROS Data Reduction System (DRS¹²) pipeline implemented in the ESO-MIDAS environment.

We obtained spectra of TYC 4515 and TYC 4946 at the Apache Point Observatory (New Mexico, US), using the ARC Echelle Spectrograph (ARCES) on the 3.5 m telescope with a resolution of $R = 31,500$ in the spectral range 3200–10000 Å. The spectra were reduced using a dedicated pipeline¹³ based on IRAF,¹⁴ then normalized to the continuum level.

TYC 4479 was observed using The Fibre-fed Échelle Spectrograph (FIES; Frandsen & Lindberg 1999; Teltung et al. 2014) on the 2.56 m Nordic Optical Telescope (Observatorio del Roque de los Muchachos, La Palma, Spain) in its *low-res* mode ($R = 25,000$, with wavelength coverage from 3700 to 7300 Å).

¹² <http://www.eso.org/sci/facilities/lasilla/instruments/feros/tools/DRS.html>

¹³ http://astronomy.nmsu.edu:8000/apo-wiki/attachment/wiki/ARCES/Thorburn_ARCES_manual.pdf and http://astronomy.nmsu.edu:8000/apo-wiki/attachment/wiki/ARCES/Kinemuchi_ARCES_cookbook.pdf

¹⁴ IRAF is distributed by the National Optical Astronomy Observatories, which are operated by the Association of Universities for Research in Astronomy, Inc., under cooperative agreement with the National Science Foundation.

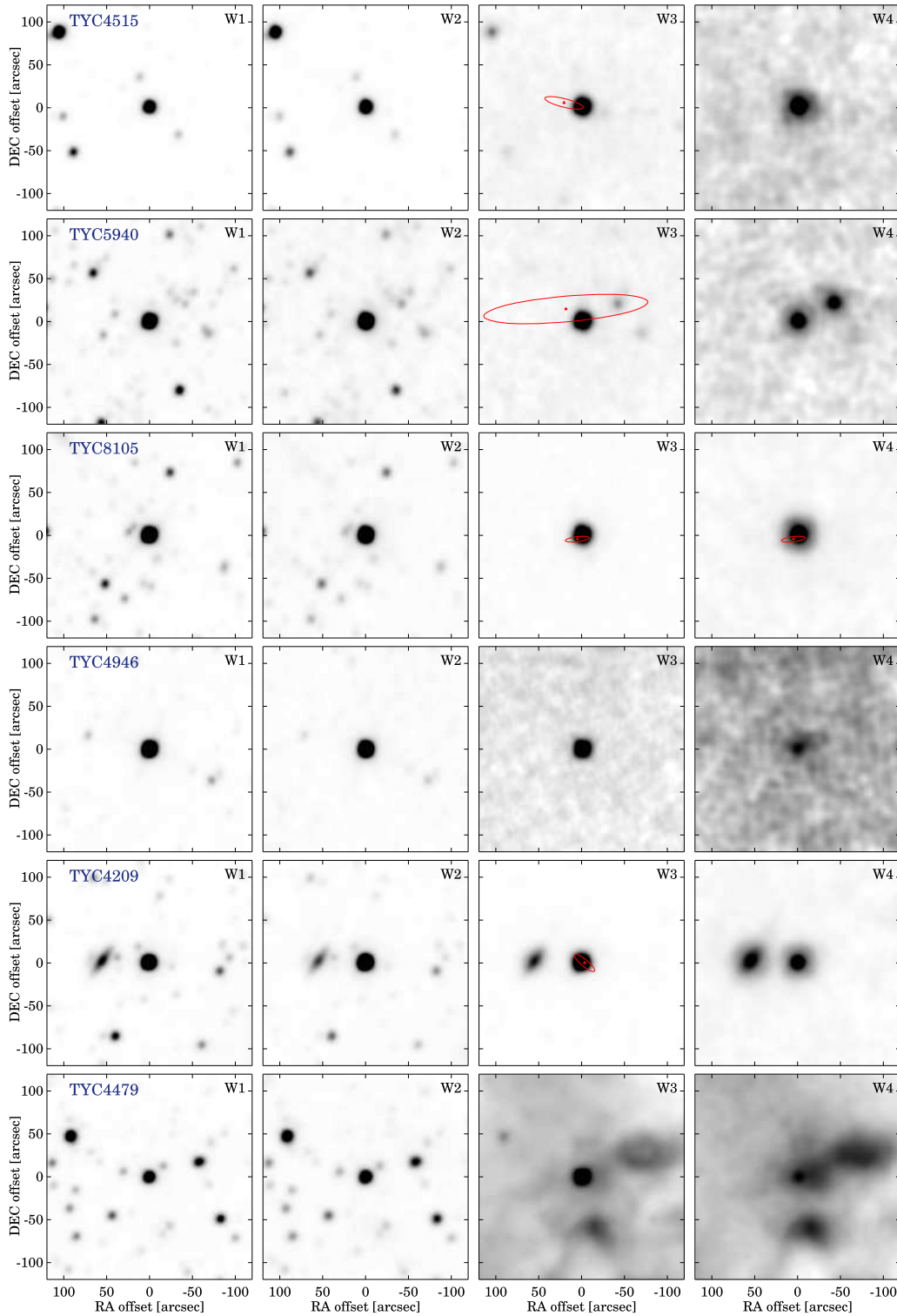


Figure 1. W1 – W4 band images (unWISE coadds of the WISE all-sky survey; see Appendix A) of the six selected objects. Positions of nearby IRAS Faint Source Catalog (FSC) point sources (marked by red plus signs) with their 1σ (3σ for TYC 5940) error ellipses are overlotted in the W3 band panels.

Data processing was made with FIESTool,¹⁵ the dedicated pipeline of the FIES instrument.

Finally, the spectrum of TYC 4209 was taken with the ACE spectrograph mounted on the 1 m RCC telescope at Pizskéstető Observatory (Hungary). The fiber-fed spectrograph covers a

range of 4150–9150 Å with a spectral resolution of $\approx 20,000$. For the wavelength calibration, a thorium–argon (ThAr) lamp was used. Data reduction was performed using standard IRAF procedures in the `imred` and `echelle` packages. Cosmic-ray correction was done by the `crutil.cosmicrays` utility. For the analysis, we combined four frames (one with a 3600 s exposure time and three with a 5400 s exposure time).

¹⁵ <http://www.not.iac.es/instruments/fies/fiestool/FIESTool.html>

Table 1
Stellar and Disk Properties

Parameters	TYC 4515	TYC 5940	TYC 8105	TYC 4946	TYC 4209	TYC 4479	References
Identifiers							
TYCHO	TYC 4515-485-1	TYC 5940-1510-1	TYC 8105-370-1	TYC 4946-1106-1	TYC 4209-1322-1	TYC 4479-3-1	Høg et al. (2000)
Gaia DR2	552973538962350080	2942418533272205312	5554553591848668672	3596395748683517440	2161325369818713984	2210856513228282496	Gaia DR2
Gaia EDR3	552973538964681088	2942418533272205312	5554553591848668672	3596395748683517440	2161325369818713984	2210856513228282496	Gaia EDR3
Astrometric information							
α R.A. (2000)	+05:04:07.2	+06:05:13.6	+06:11:03.5	+12:13:34.2	+18:17:03.9	+23:52:50.6	SIMBAD
δ Decl. (2000)	+77:58:57.5	-19:13:08.3	-47:11:29.4	-05:35:43.4	+64:33:55.0	+67:30:37.6	SIMBAD
μ_{α^*} (mas yr ⁻¹)	+6.710 ± 0.012	+0.011 ± 0.010	+6.277 ± 0.012	-27.754 ± 0.023	+12.051 ± 0.014	+38.619 ± 0.016	Gaia EDR3
μ_{δ} (mas yr ⁻¹)	-23.625 ± 0.015	-11.719 ± 0.012	+12.577 ± 0.014	-4.047 ± 0.018	-3.106 ± 0.013	-39.644 ± 0.014	Gaia EDR3
π (mas)	+3.564 ± 0.015	+3.784 ± 0.013	+5.411 ± 0.010	+4.093 ± 0.021	+3.647 ± 0.010	+6.142 ± 0.014	Gaia EDR3
RUWE ^a	0.872	0.964	0.796	1.214	0.744	0.888	Gaia EDR3
Photometric data							
B_T	11.315 ± 0.054	12.949 ± 0.258	12.486 ± 0.191	11.199 ± 0.064	12.281 ± 0.160	11.853 ± 0.078	Høg et al. (2000)
B	11.154 ± 0.100	12.694 ± 0.021	12.448 ± 0.031	11.143 ± 0.011	11.980 ± 0.133	11.769 ± 0.075	Henden et al. (2016)
BP_{Gaia}	10.8965 ± 0.0028	12.1920 ± 0.0035	11.9305 ± 0.0038	10.8298 ± 0.0028	11.7268 ± 0.0031	11.3735 ± 0.0030	Gaia EDR3
V_T	10.807 ± 0.051	11.923 ± 0.156	11.746 ± 0.136	10.921 ± 0.073	11.684 ± 0.131	11.153 ± 0.069	Høg et al. (2000)
V	10.705 ± 0.087	12.007 ± 0.070	11.696 ± 0.026	10.669 ± 0.013	11.560 ± 0.049	11.156 ± 0.048	Henden et al. (2016)
G_{Gaia}	10.6430 ± 0.0028	11.8630 ± 0.0028	11.5505 ± 0.0028	10.5926 ± 0.0028	11.4509 ± 0.0028	11.0459 ± 0.0028	Gaia EDR3
RP_{Gaia}	10.2366 ± 0.0038	11.3693 ± 0.0040	11.0042 ± 0.0042	10.2026 ± 0.0038	11.0122 ± 0.0039	10.5491 ± 0.0038	Gaia EDR3
J	9.815 ± 0.022	10.787 ± 0.024	10.426 ± 0.024	9.793 ± 0.023	10.556 ± 0.023	9.972 ± 0.023	Cutri et al. (2003)
H	9.620 ± 0.021	10.518 ± 0.022	10.028 ± 0.022	9.586 ± 0.022	10.267 ± 0.023	9.663 ± 0.031	Cutri et al. (2003)
K_s	9.538 ± 0.019	10.402 ± 0.019	9.934 ± 0.021	9.520 ± 0.023	10.139 ± 0.016	9.624 ± 0.018	Cutri et al. (2003)
Kinematics							
$v_{r,\text{our}}$ (km s ⁻¹)	+12.50 ± 0.50	+28.50 ± 0.20	+29.00 ± 0.20	-11.30 ± 0.50	-13.20 ± 0.60	+0.22 ± 0.30	This work
$v_{r,\text{Gaia}}$ (km s ⁻¹)	-2.65 ± 0.89	+30.52 ± 1.38	+29.06 ± 0.65	-12.29 ± 0.36	-13.46 ± 1.14	...	Gaia DR2
U^b (km s ⁻¹)	-32.7 ± 0.3	-8.1 ± 0.1	-16.9 ± 0.1	-27.2 ± 0.2	+3.0 ± 0.1	-21.2 ± 0.1	This work
V^b (km s ⁻¹)	-11.3 ± 0.3	-27.4 ± 0.1	-25.9 ± 0.2	-12.3 ± 0.3	-4.1 ± 0.5	-7.0 ± 0.3	This work
W^b (km s ⁻¹)	-3.7 ± 0.2	-14.5 ± 0.1	-5.8 ± 0.1	-16.5 ± 0.4	-20.1 ± 0.3	-36.2 ± 0.1	This work
Distance (pc) ^c	278.8 ± 1.1	262.1 ^{+1.2} _{-1.0}	184.1 ^{+0.4} _{-0.3}	242.1 ^{+1.4} _{-1.1}	270.8 ^{+0.7} _{-0.6}	162.0 ^{+0.4} _{-0.3}	Bailer-Jones et al. (2021)
Stellar properties							
Spectral Type	F5V	G5V	G9V	F6V	G1V	G6V	This work
T_{eff} (K)	6540 ± 100	5660 ± 100	5350 ± 100	6350 ± 60	5890 ± 120	5620 ± 100	This work
log g (cgs)	4.28 ± 0.10	4.49 ± 0.10	4.48 ± 0.10	4.13 ± 0.06	4.40 ± 0.10	4.30 ± 0.10	This work
[Fe/H] (dex)	+0.07 ± 0.10	+0.06 ± 0.10	+0.08 ± 0.10	-0.02 ± 0.05	+0.01 ± 0.12	-0.29 ± 0.10	This work
L_* (L_{\odot})	3.72 ± 0.12	0.94 ± 0.03	0.65 ± 0.02	2.55 ± 0.08	1.43 ± 0.04	0.76 ± 0.02	This work
M_* (M_{\odot})	1.32 ± 0.04	0.99 ^{+0.04} _{-0.03}	0.94 ± 0.03	1.17 ^{+0.04} _{-0.03}	1.05 ± 0.03	0.84 ± 0.03	This work
EW _{Li} (mÅ) ^d	<15.0	157 ± 8	173 ± 6	38 ± 8	101 ± 15	13 ± 4	This work
P_{rot} (day)	...	3.76	5.04	...	5.07	32.1	This work
Age (Myr)	>150	120 ± 20	130 ± 30	>150	275 ± 50	5000 ± 2000	This work
Multiplicity	Y	N	Y	Y	Y	Y	This work

Table 1
(Continued)

Parameters	TYC 4515	TYC 5940	TYC 8105	TYC 4946	TYC 4209	TYC 4479	References
Disk properties							
$T_{\text{disk,bb}}$ (K)	500 ± 25	420 ± 16	300 ± 20	680 ± 45	530 ± 15	400 ± 25	This work
f_d	0.015	0.037	0.052	0.010	0.070	0.014	This work
$R_{\text{disk,bb}}$ (au)	0.60	0.43	0.69	0.27	0.33	0.42	This work
f_d/f_{max} (10^5)	1.1	1.9	0.8	3.4	20.0	25.4	This work
Mid-IR variations	N	Y	Y	N	Y	Y	This work

Notes.

^a Renormalized Unit Weight Error (RUWE) is a quality indicator for Gaia astrometric data (for more details see the technical note GAIA-C3-TN-LU-LL-124-01, <https://www.cosmos.esa.int/web/gaia/public-dpac-documents>). RUWE values of <1.4 indicate reliable astrometric solutions.

^b In computation of the U , V , W velocity components, we used the radial-velocity data obtained by us ($v_{r,\text{our}}$).

^c Geometric distances from Bailer-Jones et al. (2021).

^d Lithium equivalent widths after correction for blending with the iron line (Section 3.4).

Table 2
Log of Spectroscopic Observations

Name	Instrument	Obs. date	Exposure time (s)
TYC 4515	ARCES	2013-03-25	780
TYC 5940	FEROS	2016-12-17	900
TYC 8105	FEROS	2016-12-17	900
TYC 4946	FEROS	2012-12-25	1022
	ARCES	2013-04-01	840
TYC 4209	ACE	2016-09-29	$3 \times 5400 + 1 \times 3600$
TYC 4479	FIES	2020-07-03	2760

3.2. Basic Stellar Properties

The preparation of the reduced spectra consisted of the identification and removal of nonspectral features remaining from the reduction processes, and a correction of the continuum normalization. These steps were carried out utilizing IRAF tasks and the iSpec tool of Blanco-Cuaresma et al. (2014). Before fitting the stellar parameters, the radial velocity had to be determined and the necessary correction had to be applied. These tasks were also performed with the iSpec tool.

For the determination of stellar parameters ($\log g$, T_{eff} , and $[\text{Fe}/\text{H}]$) of the target stars, we used the SP_Ace program (v1.1) written and developed by Boeche & Grebel (2016). SP_Ace was designed for analyzing spectra with resolution between ~ 1000 and $\sim 20,000$, but higher resolutions may be doable as well. In this range, the line profiles are plausible, since the effects of the applied approximations have been tested to not emerge. The SP_Ace methodology offers a fast and accurate solution of spectra in this range.

SP_Ace is an equivalent-width (EW) based tool (the EW library was computed by MOOG; Sneden 1973), which performs the spectral analysis under LTE assumption and based on 1D atmospheric models. It uses the General Curve-Of-Growth library (GCOG) to compute the EWs of the lines, construct models of spectra as a function of the stellar parameters and abundances, and search for a model that minimizes the χ^2 when compared to the observed spectrum. In SP_Ace, we covered the stellar parameter ranges of $3600 \text{ K} < T_{\text{eff}} < 7400 \text{ K}$, $0.2 < \log g < 5.4$, and $-2.4 \text{ dex} < [\text{Fe}/\text{H}] < 0.4 \text{ dex}$.

To use this code, the spectra must be wavelength calibrated, continuum normalized, and radial-velocity corrected at rest frame. They must be in the wavelength ranges 5212–6860 and 8400–8924 Å and must have less than 32,000 pixels. Because of the last requirement, when necessary, we downgraded the spectral resolution. To test how the precision behaves after such downgrading, we analyzed publicly available spectra of stars with well-known spectral parameters and found that there are no significant differences between the parameters derived from the spectra with different spectral resolution in the $\sim 20,000$ – $40,000$ resolution range.

The estimated stellar parameters and their uncertainties are summarized in Table 1. As a final step, the error of the radial velocity is revised with the resulting stellar parameters. The obtained radial velocities are also listed in Table 1.

In order to predict the stellar photospheric contribution to the total flux at mid-IR wavelengths, we fitted the optical and near-IR photometry of the sources (taken from Table 1) by the appropriate ATLAS9 stellar atmospheric model (Castelli & Kurucz 2004) selected based on the previously derived stellar parameters. In the fitting process, two parameters, the amplitude of the photospheric model and the interstellar reddening

(adopting the extinction curve from Cardelli et al. 1989) were estimated using a grid-based approach. Initially we used all 2MASS (Skrutskie et al. 2006) photometric data, but we found that the longest-wavelength K_s data points were systematically higher than the fitted photosphere model, suggesting that the measured fluxes are not purely photospheric. Therefore, we discarded the K_s band photometry from this analysis. Although our targets are located farther away than 160 pc, i.e., likely out of the Local Bubble, apart from the case of TYC 4515—where an $E(B - V)$ value of $0.04 \pm 0.02 \text{ mag}$ was obtained—their reddening values were found to be negligible based on this fitting. Combining these models with the Gaia EDR3 distances, we derived the stellar luminosities, also listed in Table 1.

3.3. Stellar Companions

To explore possible stellar companions, we used the Gaia EDR3 catalog to search for common proper motion and distance pairs of our targets. Following the considerations from Andrews et al. (2017), we set a limit of 1 pc for the maximum separation of the possible pairs. To ensure reliable quality astrometric solutions, we considered only stars whose parallax and proper motion measurements fulfilled the following criteria: $\pi/\sigma_\pi > 5$ and $\frac{\sqrt{\mu_{\alpha^*}^2 + \mu_\delta^2}}{\sqrt{\sigma_{\mu_{\alpha^*}}^2 + \sigma_{\mu_\delta}^2}} > 5$, respectively. We identified companions by applying the method described in Deacon & Kraus (2020), which takes into account the possible orbital motion of the components. We found probable wide-separation companions to TYC 4515, TYC 8105, TYC 4946, TYC 4209, and TYC 4479, i.e., to all stars with the exception of TYC 5940. All of the companion stars have $\text{RUWE}^{16} < 1.4$, indicating a well-fitting astrometric solution. Despite the large search radius, the projected separations of the identified pairs range between 1000 ($\sim 0.005 \text{ pc}$) and 6000 au ($\sim 0.03 \text{ pc}$). This means that both components can be formed by the fragmentation of a single protostellar core, which has a typical size of 0.1 pc (Lada et al. 2008; Duchêne & Kraus 2013). Table 3 shows the astrometric parameters for the five pairs.

For the companions of TYC 4515, TYC 8105, TYC 4209, and TYC 4479, we estimated the effective temperatures based on their $r - z$, $r - J$, and $G_{BP} - G_{RP}$ color indices, using the calibration derived by Mann et al. (2015). The G_{BP} - and G_{RP} -band data were collected from the Gaia EDR3 catalog. The J -band measurements were extracted from the 2MASS survey (Skrutskie et al. 2006). For TYC 8105B, the r - and z -band photometry were taken from The Dark Energy Survey (DR1; Abbott et al. 2018), while in the cases of TYC 4515B and TYC 4209B, magnitudes measured in The Pan-STARRS Survey (DR1; Chambers et al. 2016) were transformed into the SDSS system using the equations presented in Tonry et al. (2012). For TYC 4209B, which was observed both in The SDSS Photometric Catalog (Release 12, Alam et al. 2015) and The Pan-STARRS Survey, we derived the final r - and z -band photometry as the weighted average of these data (after the transformation of the Pan-STARRS observations to the SDSS photometric system). Photometry for TYC 4515B were dereddened by adopting the $E(B - V)$ values obtained for their primary components (Section 3.2). The final T_{eff} values, which

¹⁶ Renormalized Unit Weight Error (RUWE) is an indicator of the goodness of fit for Gaia astrometric data: values < 1.4 are considered reliable (for more details, see the technical note GAIA-C3-TN-LU-LL-124-01, <https://www.cosmos.esa.int/web/gaia/public-dpac-documents>).

Table 3
Astrometric Parameters and Stellar Properties of the Probable Common Motion and Distance Pairs

Name	Gaia EDR3 ID	Separation (au)	μ_{α^*} (mas yr ⁻¹)	μ_{δ} (mas yr ⁻¹)	π (mas)	G (mag)	SpT	T_{eff} (K)	L_* (L_{\odot})	M_* (M_{\odot})
TYC 4515B	552973534667883904	1825	+6.61 ± 0.05	-24.18 ± 0.08	3.49 ± 0.06	16.578	M1	3670 ± 60	0.0363 ± 0.0014	0.50 ± 0.02
TYC 8105B	5554553527426091136	4540	+6.80 ± 0.33	+13.54 ± 0.39	5.57 ± 0.30	19.510 ^a	M5.5	2960 ± 60	0.0024 ± 0.0001	0.096 ± 0.01
TYC 4946B	3596395748685297792	1010	-27.66 ± 0.34	-5.07 ± 0.26	4.08 ± 0.28	18.812 ^a	M4.5	~3120	~0.005	~0.19
TYC 4209B	2161326842991191936	6010	+12.13 ± 0.17	-3.38 ± 0.17	3.85 ± 0.11	18.337	M3.5	3230 ± 55	0.0077 ± 0.0003	0.27 ± 0.01
TYC 4479B	2210856513228282880	5040	+38.90 ± 0.04	-39.53 ± 0.04	6.12 ± 0.03	15.867	M2	3540 ± 60	0.0182 ± 0.0006	0.38 ± 0.02

Note.

^a Corrected G -band magnitude for sources with six-parameter astrometric solutions based on Riello et al. (2020).

∞

are the weighted averages of the three T_{eff} estimates corresponding to the three colors, are listed in Table 3.

The spectral types of the companions were estimated based on the obtained effective temperatures using an updated version¹⁷ of the conversion from Pecaut & Mamajek (2013). We found that the spectral types of these secondary components range between M1 and M5.5; thus, these are newly discovered M dwarfs. We also derived the stellar luminosities. As a first step, we performed bolometric correction to the G , r , z , J , H , and K_s passbands using the proper equations of Mann et al. (2015). The final bolometric magnitudes were obtained as the weighted average of the six individual bolometric magnitudes. Then, considering the reddening and adopting the distances of the primary components (which have substantially lower uncertainties than those of the companions), we calculated the luminosities of the four companions (Table 3).

For TYC 4946B, where reliable photometry was available only in the G band, the T_{eff} , L_* , and M_* parameters and the spectral type were estimated based on its G -band absolute magnitude by interpolating in the updated table of Pecaut & Mamajek (2013). The obtained parameters of this \sim M4.5-type star are also listed in Table 3.

We also investigated the possible existence of closer binary pairs in our sample. Qian et al. (2019) listed TYC 4946 as a possible spectroscopic binary, because its two observations in the Large Sky Area Multi-Object Fiber Spectroscopic Telescope survey brought very different radial-velocity measurements ($v_r = -37.99 \pm 0.72 \text{ km s}^{-1}$ and $-16.30 \pm 3.43 \text{ km s}^{-1}$). For this star, we obtained radial velocities of -10.5 ± 0.7 and $-12.1 \pm 0.7 \text{ km s}^{-1}$ from the observations carried out by the ARCES and FEROS spectrographs at two different epochs (Table 2). The Gaia DR2 catalog (Gaia Collaboration et al. 2018b)—in good agreement with our results—quotes a v_r of $-12.29 \pm 0.36 \text{ km s}^{-1}$. In the case of TYC 4515, we extracted v_r of $+12.5 \pm 0.5 \text{ km s}^{-1}$ from our high-resolution spectrum (Table 1), which deviates significantly from its v_r of $-2.65 \pm 0.89 \text{ km s}^{-1}$ as measured by Gaia. These two stars are candidate spectroscopic binaries, but further measurements are needed to confirm this claim. If TYC 4515 or TYC 4946 has a spectroscopic binary pair, then they would be triple systems. For TYC 5940, TYC 8105, and TYC 4209, our v_r measurements are consistent with the Gaia-derived values; thus, there is no indication for any close companion.

3.4. Age of the Stars

The ages of the host stars provide important information in assessing the evolutionary status of their disks. To infer this parameter, we combined a variety of age diagnostics based on lithium content, stellar rotation, and kinematic properties. In the case of TYC 8105, isochrone fitting for its M-type companion was also performed.

In stars having a convective layer, as in our objects, photospheric lithium is thought to be depleted with time when mixed into deeper layers due to convection, and destroyed at a temperature of about $2.5 \times 10^6 \text{ K}$. We measured the lithium content using the resonance doublet of Li I at 6707.7 \AA , whose equivalent widths (EW_{Li}) were measured by fitting a Gaussian profile to the absorption feature in our high-resolution spectra (see Section 3.1). The Li absorption line is blended with a weak

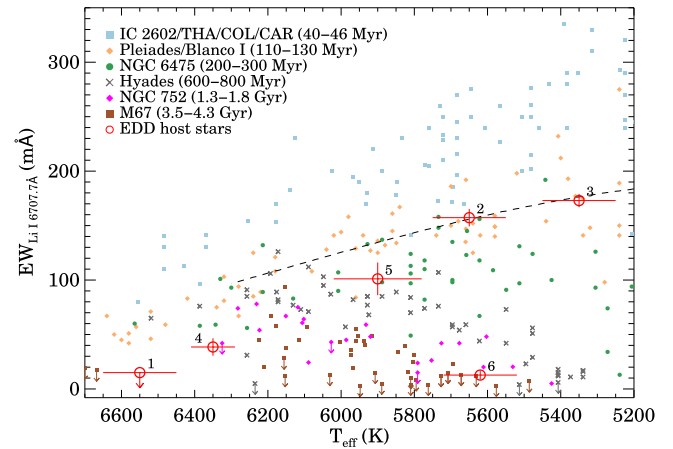


Figure 2. Equivalent width of the lithium line (at 6707.7 \AA) as a function of effective temperature for our targets (1: TYC 4515, 2: TYC 5940, 3: TYC 8105, 4: TYC 4946, 5: TYC 4209, 6: TYC 4479) and for members of some nearby open clusters and moving groups with well-known ages. Data for open clusters were taken from Sestito & Randich (2005) via the WEBDA database (<https://webda.physics.muni.cz/>), while for the Tucana-Horologium (THA), Columba (COL), and Carina (CAR) moving groups, the data were taken from da Silva et al. (2009). The dashed curve represents a polynomial fit to the lithium data of Pleiades (Pecaut & Mamajek 2016). Ages of moving groups and open clusters were taken from the literature: IC 2602 (Dobbie et al. 2010); THA, COL, and CAR (Bell et al. 2015); Pleiades (Stauffer et al. 1998; Dahm 2015); Blanco I (Cargile et al. 2010; Juarez et al. 2014); NGC 6475 (Villanova et al. 2009; Cummings & Kalirai 2018; Bossini et al. 2019); Hyades (Douglas et al. 2019, and references therein); NGC 752 (Daniel et al. 1994; Twarog et al. 2015; Agüeros et al. 2018); and M 67 (VandenBerg & Stetson 2004; Giampapa et al. 2006; Sarajedini et al. 2009; Bossini et al. 2019).

Fe I line at 6707.4 \AA . Taking into account this effect, the obtained equivalent widths were corrected using a method developed by Soderblom et al. (1993). For TYC 4946, more than one spectrum were available, and the final EW_{Li} was computed as the average of the individual measurements. For TYC 4515, where the lithium line was not detected, a 3σ upper limit was calculated. The corrected EW_{Li} values are given in Table 1 and displayed as a function of effective temperatures in Figure 2. For comparison, members of some well-dated nearby open clusters and moving groups, representing an age range of ~ 40 – 4300 Myr , are also plotted.

Late-type dwarf stars lose mass and angular momentum via magnetized stellar winds, leading to rotational spin down as they age (Schatzman 1962; Kraft 1967; Kawaler 1988). This enables the use of stellar rotation to estimate the ages of stars via a technique called gyrochronology (Barnes 2003). Starspots may cause periodic light changes from which the rotation period can be derived. In our sample, five stars (TYC 4515, TYC 5940, TYC 8105, TYC 4209, and TYC 4479) were observed with the TESS satellite, providing high-accuracy photometry with 30 minutes cadence. All five stars exhibit periodic variations likely due to rotational modulation by starspots. By performing a frequency analysis, we obtained rotational periods as listed in Table 1. A detailed description of the TESS data reduction and the frequency analysis is given in Appendix B. In Figure 3 we plot the rotational periods as a function of the effective temperatures for those four G-type stars for which gyrochronology is applicable. Due to rotational evolution, stellar groups of different ages populate distinct, well-defined areas in this plot, as demonstrated for four open clusters: Pleiades ($\sim 120 \text{ Myr}$), Hyades and Praesepe (both

¹⁷ https://www.pas.rochester.edu/~emamajek/EEM_dwarf_UBVIJHK_colors_Teff.txt

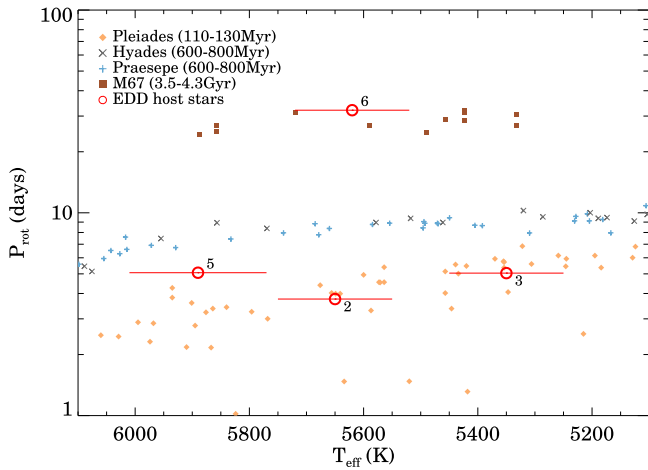


Figure 3. Rotation periods as a function of effective temperatures for our targets and for single star members of three open clusters. Our targets (TYC 5940, TYC 8105, TYC 4209, and TYC 4479) have the same labels as in Figure 2. Data for open cluster members were taken from the literature (Barnes et al. 2016; Rebull et al. 2016; Stauffer et al. 2016; Douglas et al. 2019).

600–800 Myr), and M67 (3.8–4.3 Gyr). Having similar ages, the members of Hyades and Praesepe overlap in this diagram.

By comparing the effective temperatures and luminosities of the six host stars (Table 1) and the four companions (Table 3) with the corresponding mean properties of dwarf stars,¹⁸ we found that all, but TYC 8105 B, are consistent with the main sequence. TYC 8105 B is brighter than main-sequence dwarfs with comparable T_{eff} , suggesting that it is in pre-main-sequence evolution. To verify the age estimate of the TYC 8105 system, we performed isochrone fitting (see below) for the companion using isochrone tracks constructed by Baraffe et al. (2015).

Using astrometric data (coordinates, proper motions, and trigonometric parallax) from the Gaia EDR3 catalog, supplemented by our radial-velocity measurements from Table 1, we computed the U , V , and W Galactic space velocity components of the targets. In this calculation, we used a right-handed coordinate system; thus, U is positive toward the Galactic center, V is positive in the direction of Galactic rotation, and W is positive toward the Galactic north pole. The derived Galactic space velocities are listed in Table 1 and displayed in Figure 4. For TYC 4515 and TYC 4946 where some radial-velocity data in the literature differ substantially from our measurements (Section 3.3), the UVW components were computed also using the most different v_r data, and they are displayed in Figure 4. For reference, known moving groups, associations, and open clusters located within 300 pc are also plotted.

TYC 5940 and TYC 8105 are both G-type stars (Table 1). As Figure 2 demonstrates, their lithium equivalent widths are consistent with the Pleiades stars (~ 120 Myr), and lower than the values measured in the 40–50 Myr old members of nearby moving groups and of the IC 2602 open cluster.

In line with this, the position of both stars in the period-effective temperature diagram (Figure 3) also matches the sequence of the Pleiades. To estimate the gyrochronology age, we applied four different calibrations for the rotation–age relation (Barnes 2007; Mamajek & Hillenbrand 2008; Meibom et al. 2009; Angus et al. 2015). For TYC 5940, these calibrations yielded age estimates between 92 and 134 Myr with an average

of 118 Myr, while the gyro ages for TYC 8105 range from 125 to 197 Myr with an average of 163 Myr.

As Figure 4 outlines, the UVW velocities of both stars are consistent with the typical space motion of nearby young (10–200 Myr old) stars. Interestingly, the derived U , V , W components of TYC 5940 overlap with the Pleiades and the AB Dor moving groups. We note, however, that the direction and distance of this star are clearly inconsistent with those of both Pleiades and the currently known values of the AB Dor group, making its membership unlikely.

According to our analysis, TYC 8105 has a wide-separation M5.5-type pre-main-sequence companion. To determine its best-fit mass and isochrone age, we followed the Bayesian inference approach outlined in Pascucci et al. (2016) for the comparison of the measured L_* and T_{eff} parameters (from Table 3) with theoretical predictions from Baraffe et al. (2015). We obtained an isochrone age of 75_{-30}^{+50} Myr. Although somewhat lower, this age estimate is consistent with the lithium and gyro ages within the uncertainties. In fact, isochrones of Baraffe et al. (2015) are available only for solar metallicity, while TYC 8105 is a bit more metal-rich at $[\text{Fe}/\text{H}] \sim 0.08$, which might lead to a slight underestimation of age. Moreover, isochronal model tracks tend to underestimate the age of low-mass pre-main-sequence stars (e.g., Pecauc & Mamajek 2016).

Taking into account the results of the different methods, we adopted ages of 120 ± 20 Myr and 130 ± 30 Myr for TYC 5940 and TYC 8105, respectively.

TYC 4209 falls between the Pleiades (~ 120 Myr) and Hyades stars (600–800 Myr old) in Figure 2, and its measured EW_{Li} value makes it similar to members of the 200–300 Myr old open cluster NGC 6475 (Villanova et al. 2009; Cummings & Kalirai 2018; Bossini et al. 2019). The obtained P_{rot} of 5.07 days also places the star between the sequences of Pleiades and Hyades/Praesepe in the period– T_{eff} plot (Figure 3). The average of the gyro-age estimates is 295 Myr with a range between 241 and 333 Myr. That this object is somewhat older than the previous two stars is also supported by its location in Figure 4 outside the region of the young, 10–200 Myr old groups. Based on these results, we adopted an age of 275 ± 50 Myr for TYC 4209.

TYC 4515 and TYC 4946 are the hottest stars in our sample. Studying the Li abundances in different open clusters showed that similar mid-F-type members with effective temperatures between 6300 and 6900 K often have significant lithium depletion compared to co-eval but somewhat colder or hotter stars (e.g., Boesgaard & Tripicco 1986; Balachandran 1995). This so-called Li dip has not been observed in the Pleiades, but according to Steinhauer & Deliyannis (2004), it already appears at an age of ~ 150 Myr. The measured EW_{Li} values for TYC 4946 and especially for TYC 4515 are significantly lower than those of Pleiades stars, implying a serious Li depletion and suggesting a lower limit of 150 Myr for their ages. Although the Galactic velocity components of both stars are quite uncertain due to the uncertainty of radial velocities (Section 3.3), in the case of TYC 4946, the possible U , V , W range mostly deviates from the one typical for nearby young stars (Figure 4), further supporting this age estimate. Considering all results, we adopted a lower limit of 150 Myr for both systems.

TYC 4479 has a lithium EW lower than those of the similar-temperature members of NGC 752 (1.3–1.8 Gyr) and roughly consistent with the upper limits measured for late-G-type stars belonging to the ~ 4 Gyr old M67 open cluster (Figure 2). In its

¹⁸ http://www.pas.rochester.edu/~emamajek/EEM_dwarf_UBVJHK_colors_Teff.txt (compiled by E. Mamajek).

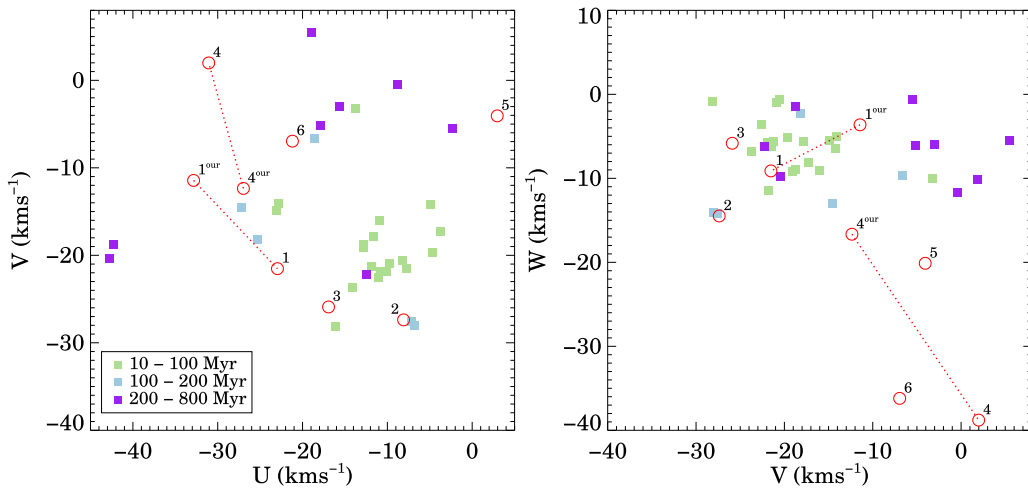


Figure 4. (U, V) - and (V, W) -planes for the host stars of extreme debris disks (red circles). For TYC 4515 and TYC 4946, correspondingly to the measured v_r range, two U, V, W values are shown (Section 3.4). 1: TYC 4515, 2: TYC 5940, 3: TYC 8105, 4: TYC 4946, 5: TYC 4209, and 6: TYC 4479. Filled squares display space velocities of known moving groups, associations, and open clusters located within 300 pc taken from the literature (Gagné et al. 2018; Soubiran et al. 2018). Different colors stand for different age ranges.

TESS light curve, we found a variation with a period of ~ 32 days and an amplitude of ~ 0.0012 mag. The observed period is slightly longer than the rotational periods observed for late-G stars of M67 (Figure 3). Assuming that the observed changes are also related to stellar rotation, the above-mentioned gyrochronologic relations yield age estimates between 5.4 and 6.5 Gyr, with a mean of 6 Gyr, for TYC 4479. However, the calibrations of gyrochronology are based on well-dated stars—typically members of open clusters and moving groups—whose metallicity differs only marginally from that of Sun, while TYC 4479 has an $[\text{Fe}/\text{H}]$ of -0.29 . According to Amard & Matt (2020), this could have a significant effect: the rotation of such a metal-poor star is expected to be faster than a similar mass star with a solar metallicity. This can lead to an underestimation of the stellar age using the available gyrochronology relations. As Figure 4 demonstrates, the W velocity component of the star differs significantly from the typical W of nearby stellar groups younger than 800 Myr. By applying a recent age–velocity relation proposed by Almeida-Fernandes & Rocha-Pinto (2018), we compiled a probability density function for the age of a star based on its UVW data. Based on this, the kinematic age is $4.8_{-1.6}^{+5.7}$ Gyr. All of these results indicate that TYC 4479 is definitely older than 2 Gyr, and its age is likely at least comparable to that of the Sun. For this star, we adopted an age of 5 ± 2 Gyr.

All six systems are found to be older than 100 Myr, implying that the observed dust cannot be primordial material but rather is of secondary origin, i.e., these stars host EDDs.

Using the obtained luminosity, effective temperature, and metallicity parameters (Table 1), we estimated the mass of the host stars based on the PARSEC evolutionary models (ver. 1.2S, Bressan et al. 2012). In this analysis, we took into account the estimated ages of the stars as a priori information. The resulting stellar masses are listed in Table 1. Using the same approach, we also estimated the masses of the companions. For TYC 4515B, TYC 4209B, and TYC 4479B, we used the PARSEC models, while for the late-M-type TYC 8105B, the evolutionary models were taken from Baraffe et al. (2015). For these objects, we assumed metallicities and ages similar to those of the primary components. The obtained stellar masses are listed in Table 3.

4. Characterization of the Disks

4.1. WISE Observations

The primary survey of WISE is comprised of three phases. In the first 7 months of the survey operation (between 2010 January and August), the satellite performed observations in all four bands (4-Band Cryo Phase), scanning the sky 1.2 times before the exhaustion of frozen hydrogen from its outer cryogen tank. This phase was followed by a short (~ 2 months) operational period when the focal plane was cooled by the inner cryogen system, permitting the scanning of $\sim 30\%$ of the sky in the W1, W2, and W3 bands (3-Band Cryo Phase). Finally, after the end of the cryogenic mission, in the framework of the NEOWISE Post-Cryo survey phase, approximately 70% of the sky was observed in the W1 and W2 bands, achieving thereby a complete second coverage of the sky at the shortest wavelengths. At the close of this phase, the satellite was put into hibernation in 2011 February. In 2013 October, the spacecraft was reactivated, and sky surveys were continued in the W1 and W2 bands. The recent NEOWISE 2020 Data Release provides photometric data obtained in the first 6 yr of the Reactivation survey, during which the satellite scanned the sky approximately 12 times.

By gathering single-exposure observations obtained for our targets during the above-mentioned survey phases from the NASA/IPAC Infrared Science Archive (IRSA) database, we could extract W1 and W2 photometric data clustered in 14–15 observational windows. Apart from a larger gap due to the hibernation period, these windows are typically spaced by ~ 6 months. In the case of TYC 4479, these data are completed by W3 and W4 band photometry in the first two epochs. For the remaining sources, these long-wavelength data are only available in the first epoch. Corresponding to the applied observing strategy of WISE (Wright et al. 2010), the individual observing windows of our targets are 0.7–34 days long with 10–300 single-exposure measurements depending mainly on the ecliptic latitude of the source.

In the following analysis, we used only the best-quality single-exposure data points and discarded measurements where the frameset images had low quality ($qi_fact = 0$).

Following the Explanatory Supplement¹⁹ in order to filter out framesets that could be contaminated by higher levels of charged particle hits or by scattered moonlight, we removed data points where the frameset was taken when the satellite was located within the nominal boundaries of the South Atlantic Anomaly ($saa_sep < 5$) or was performed within an area close to the Moon ($moon_masked = 1$). We also removed all measurements having contamination and confusion flags (cc_flags) of either “D,” “P,” “H,” “O,” “L,” or “R.” Moreover, we found that data points where the reduced χ^2 of the profile-fit photometry measurement ($wlrchi2$ or $w2rchi2$) was higher than 5 were frequently outlying from the bulk of the data, and therefore we rejected them as well.

4.2. Additional Infrared Data

To expand our knowledge on the SED of the sources, we searched for additional IR data in the literature. Using the IRAS Point Source (Helou et al. 1988) and Faint Source (FSC; Moshir 1990) catalogs, we found possible counterparts for four of our targets (TYC 4515, TYC 4209, TYC 8105, and TYC 5940) in the FSC. For TYC 4515, TYC 4209, and TYC 8105, the association with the nearby FSC source is unambiguous, since these targets are situated within the 1.5σ IRAS error ellipse, and their WISE W3 band images show no other potentially contaminating objects in their environment (Figure 1). Based on the IRAS error ellipse plotted over on the W3 band image (Figure 1), in the case of TYC 5940, an additional fainter object, to the northwest of our target, can also contribute to the measured IRAS flux. TYC 8105 was detected both at 12 and 25 μm ; for the other three sources, only 12 μm photometry is available.

For TYC 4209, an additional data point at 9 μm is available in the AKARI infrared camera (IRC) catalog (Ishihara et al. 2010). TYC 4515 was serendipitously covered by a 24 μm map obtained with the Multiband Imaging Photometer for Spitzer camera (MIPS; Rieke et al. 2004; AOR: 15184640, PI: David Jewitt). In the latter case, MIPS images produced via the Enhanced Basic Calibrated Data (EBCD) pipeline (version S18.12.0) were downloaded from the Spitzer Heritage Archive, and the MOsaicking and Point source Extraction (MOPEX) software package (Makovoz & Marleau 2005) was used to create a mosaic from the individual frames. Then point spread function (PSF) photometry was applied to obtain the flux density of TYC 4515. The source has a positional offset of $0''.55$ with respect to the proper motion corrected Gaia EDR3 position of the star. The final photometric uncertainty was derived as the quadratic sum of the measurement noise and the conservative absolute calibration uncertainty of the MIPS 24 μm array (4%, MIPS Instrument Handbook²⁰). As a result, we obtained a flux density of 25.2 ± 1.4 mJy at 24 μm .

TYC 4479, which is located in the foreground of the Cep OB4, was observed at 3.6 and 4.5 μm in a mapping project that targeted this association with the Infrared Array Camera (IRAC) instrument of Spitzer (AOR: 68515840, PI: Joseph Hora). We performed aperture photometry using those six “corrected BCD” (cBCD) images that cover our target. The aperture radius was set to 3 pixels ($3''.66$), the sky background was computed in an annulus between 12 and 20 pixels. The

background was estimated using an iterative sigma-clipping method, where the threshold was set to 3σ . We applied aperture correction with a factor of 1.113 (IRAC Instrument Handbook²¹) in both filters. Array location- and pixel phase-dependent photometric corrections were also done using the recipe from the IRAC Instrument Handbook. Finally, the six flux density values obtained in the different frames were averaged to get the final photometry. This approach yielded flux densities of 43.6 ± 0.9 mJy and 29.9 ± 0.6 mJy at 3.6 μm and 4.5 μm , respectively. The quoted uncertainties are quadratic sums of the measurement errors and the absolute calibrational uncertainty (2%, IRAC Documentation²²).

4.3. Disk Properties

To estimate the basic disk properties, we fitted a single temperature blackbody model to the observed IR excess calculated as the difference between the measured flux densities and the predicted photosphere. Mid-IR light curves showed evidence of variability at several EDDs (Melis et al. 2012; Meng et al. 2012, 2015; Su et al. 2019b). To avoid combining data points potentially related to different disk states, for the fitting process, we used only the weighted averages of W1 – W4 band WISE single-exposure photometry obtained in the first observing window of the satellite’s primary mission. While the AllWISE catalog combines data from the WISE cryogenic and NEOWISE post-cryogenic survey phases, our selected measurements form a homogeneous and simultaneously obtained data set in all four WISE filters. The uncertainties of the measured flux densities were calculated as the quadratic sum of the calibration errors (WISE All-Sky Release Explanatory Supplement Section 4.4²³) and the errors of the weighted averages. In the computation of uncertainties of the excesses, the uncertainties of the predicted photospheric fluxes were estimated to be 3% and added quadratically to the previously derived errors.

Since the SED shapes differ from the $F_\nu \propto \nu^{-2}$ reference spectrum used in the WISE catalog, the measured flux densities need to be color corrected. The color-correction factors (f_{cc}) were computed based on a simple SED model (derived as the sum of the stellar photosphere and a blackbody fitted to the excess computed from the original data). The f_{cc} values were less than 1%, except the wide bandpass W3 measurements, where they could be as high as 10%. The color-corrected WISE flux densities are plotted in Figure 5.

The SED of the disk was computed as the excess above the photosphere (Figure 5). In order to select the best-fitting blackbody model, we applied a Levenberg–Marquardt algorithm (Markwardt 2009) using the characteristic dust temperature and the solid angle of the emitting region as free parameters. Color correction of other available IR data points (Section 4.2) was also performed using the above models. Table 4 summarizes the color-corrected IR photometric data for all six objects. The obtained dust temperatures and fractional dust luminosities are listed in Table 1. Temperatures fall between 300 and 680 K, while fractional luminosities range from 0.01 to 0.07. Figure 5 shows that the WISE data points at

¹⁹ wise2.ipac.caltech.edu/docs/release/allwise/expsup/

²⁰ <https://irsa.ipac.caltech.edu/data/SPITZER/docs/mips/mipsinstrumenthandbook/>

²¹ <https://irsa.ipac.caltech.edu/data/SPITZER/docs/irac/iracinstrumenthandbook/>

²² <https://irsa.ipac.caltech.edu/data/SPITZER/docs/irac/warmingcharacteristics/>

²³ http://wise2.ipac.caltech.edu/docs/release/allsky/expsup/sec4_4.html#CalibrationU

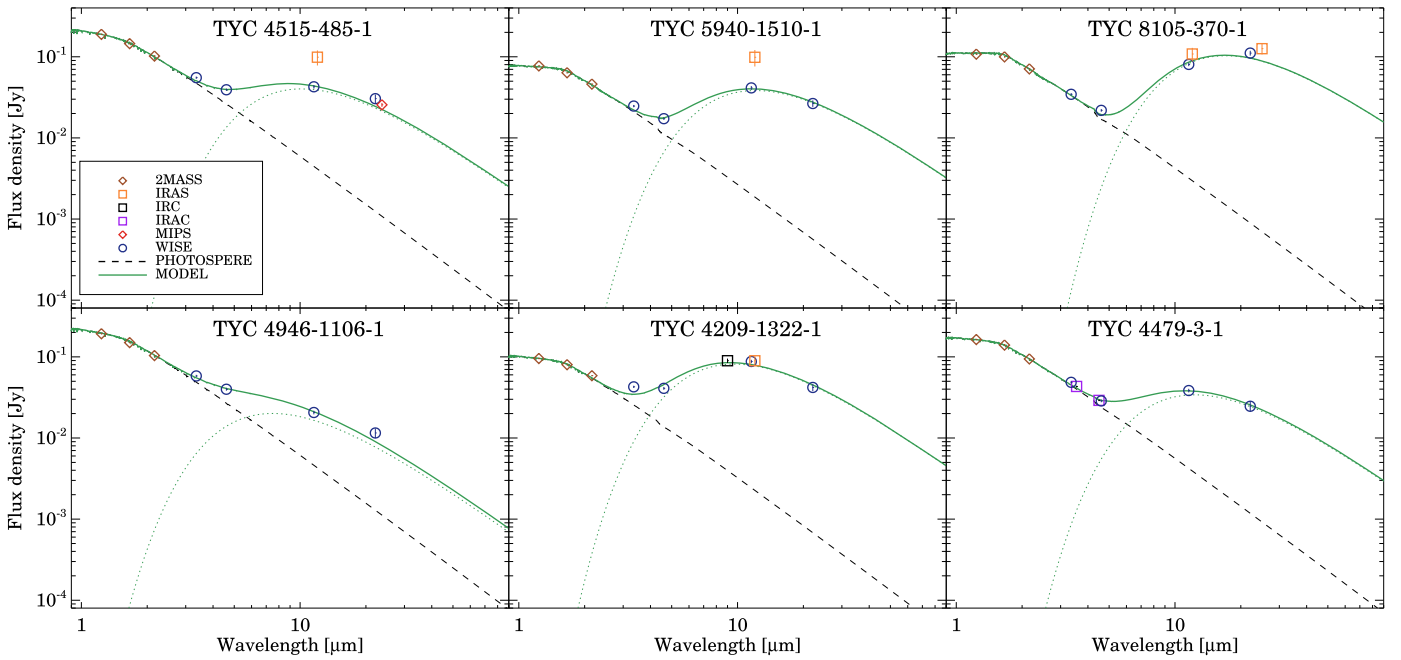


Figure 5. Color-corrected SEDs overplotted with the photosphere and disk models. Model parameters are given in Table 1.

$3.4 \mu\text{m}$ are systematically higher than the model fit. In the case of TYC 4209, the measured flux density in the W1 band is 5.5σ higher than the model fit, which likely indicates the presence of a hotter dust component in the disk. For the rest of the sample, the deviations between the measured fluxes and the models are less than 3σ . Nevertheless, it cannot be excluded that some of these disks contain additional even hotter dust as also suggested by color temperatures derived from W1, W2 data (see Figure 7).

Assuming an optically thin circumstellar dust ring with grains radiating like blackbodies, the ring radius can be calculated from the dust temperature and the stellar luminosity as $R_{\text{bb}}[\text{au}] = \left(\frac{L_{\text{star}}}{L_{\odot}}\right)^{0.5} \left(\frac{278 \text{ K}}{T_{\text{dust}}}\right)^2$. The derived blackbody radii range from ~ 0.3 to 0.7 au (Table 1).

Several caveats are associated with our simple approach. EDDs tend to show strong solid-state emission features (Olofsson et al. 2012). Without any mid-IR spectral information, we do not know how the presence of such features modifies the shape of the SED. Furthermore, in the estimation of disk radii, we assumed large grains, behaving as blackbodies, and did not account for smaller particles that are ineffective emitters and thus become hotter compared to larger grains at the same location. The derived high fractional luminosity values ($\gtrsim 0.01$) indicate that the dust may be at least partly optically thick along the line of sight, which was also not considered in our simple model.

5. Disk Variability

The available IR data allow us to assess the mid-IR variability of the sources on several different timescales. Using single-exposure WISE data, we searched for flux changes on daily and annual timescales. For those sources where additional earlier IR photometry is available (IRAS, AKARI, Spitzer), we could also investigate variability on decadal timescales.

5.1. Exploring the Annual Variability in W1/W2

To search for flux changes occurring on timescales of years, we used all single-exposure W1 and W2 band data points not discarded in the quality check. We employed two different discriminants: the correlation-based Stetson J index (S_J , Stetson 1996) and the scatter-based χ^2 test (Sokolovsky et al. 2017). By quantifying correlation of variability in two or more bands, the Stetson J index provides a robust metric to search for brightness changes. Including the W1 and W2 bands, this index can be computed as:

$$S_J = \frac{\sum_{k=1}^n w_k \text{sgn}(P_k) \sqrt{|P_k|}}{\sum_{k=1}^n w_k}, \quad (2)$$

where n is the number of paired observations taken at the same time, and w_k is the weight of the k th epoch (set to 1 uniformly in our case). P_k is the product of the normalized residuals of two observations, $P_k = \left(\sqrt{\frac{n}{n-1}} \frac{W_{1,k} - \bar{W}_1}{\sigma_{W_{1,k}}}\right) \left(\sqrt{\frac{n}{n-1}} \frac{W_{2,k} - \bar{W}_2}{\sigma_{W_{2,k}}}\right)$, where $W_{1,k}$ and $W_{2,k}$ are the k th measured magnitudes in the given bands, $\sigma_{W_{1,k}}$ and $\sigma_{W_{2,k}}$ are their uncertainties, while \bar{W}_1 and \bar{W}_2 are the means of the measured data points in the given bands. We also searched for variability in individual bands by computing the value of χ^2_{red} as

$$\chi^2_{\text{red}} = \frac{1}{N-1} \sum_{k=1}^n \left(\frac{W_k - \bar{W}}{\sigma_{W_k}}\right)^2, \quad (3)$$

where W_k and σ_{W_k} are the measured magnitudes and their uncertainties in the specific band.

To define S_J and χ^2_{red} cutoff values for separating variable objects from non-variable ones, we used an empirical approach. We selected all objects from the AllWISE catalog that (1) are located within 2° of our targets (thus have similar time sampling), (2) have W2 band magnitudes within $\pm 1.0 \text{ mag}$ to that of the specific EDD, and (3) are not marked by any

Table 4
Measured and Predicted Flux Densities

Name	Instr.	Epoch	λ (μm)	P_ν^a (mJy)	F_ν^b (mJy)
TYC 4515	WISE	2010	3.35	47.3	55.3 ± 1.7
	WISE	2010	4.60	26.1	39.2 ± 1.3
	WISE	2010	11.56	4.5	42.7 ± 2.1
	IRAS	1983	12.00	4.1	98.9 ± 20.8
	WISE	2010	22.09	1.2	30.5 ± 3.7
	MIPS	2006	23.67	1.1	25.6 ± 1.4
TYC 5940	WISE	2010	3.35	21.0	24.7 ± 0.8
	WISE	2010	4.60	11.0	17.3 ± 0.6
	WISE	2010	11.56	2.0	41.3 ± 2.3
	IRAS	1983	12.00	1.9	98.6 ± 22.7
	WISE	2010	22.09	0.6	26.5 ± 2.4
TYC 8105	WISE	2010	3.35	33.3	34.5 ± 1.2
	WISE	2010	4.60	16.8	21.9 ± 0.8
	WISE	2010	11.56	3.2	80.5 ± 3.9
	IRAS	1983	12.00	3.0	108.2 ± 20.6
	WISE	2010	22.09	0.9	111.0 ± 7.6
	IRAS	1983	25.00	0.7	125.9 ± 18.9
TYC 4946	WISE	2010	3.35	48.8	58.2 ± 1.9
	WISE	2010	4.60	26.8	39.9 ± 1.6
	WISE	2010	11.56	4.6	20.6 ± 1.1
	WISE	2010	22.09	1.3	11.5 ± 1.6
TYC 4209	WISE	2010	3.35	25.6	42.7 ± 1.4
	WISE	2010	4.60	13.6	40.9 ± 1.6
	IRC	2006	9.00	4.0	89.6 ± 5.5
	WISE	2010	11.56	2.4	87.7 ± 4.2
	IRAS	1983	12.00	2.3	89.5 ± 12.5
	WISE	2010	22.09	0.7	41.9 ± 4.1
TYC 4479	WISE	2010	3.35	45.8	48.4 ± 1.6
	IRAC	2019	3.55	41.3	43.1 ± 0.9
	IRAC	2019	4.49	25.5	29.0 ± 0.6
	WISE	2010	4.60	24.2	28.5 ± 1.0
	WISE	2010	11.56	4.4	38.4 ± 1.9
	WISE	2010	22.09	1.2	24.6 ± 3.5

Notes.

^a Predicted photospheric flux densities.

^b Measured flux densities. The quoted values are color corrected.

contamination flag in the W1 and W2 bands (“cc_flg” = 0). We gathered all single-exposure photometric data for the selected objects and compiled their light curves by applying the same quality criteria as for our targets (see Section 4.1). Finally we computed the S_J and χ_{red}^2 values for the light curves and compiled the histograms of variability indices for all studied regions independently. The obtained histograms typically show asymmetric behavior with a tail at positive values (see, e.g., Figure 6 for the case of TYC 5940). Supposing that the majority of objects show no significant variations, this finding is consistent with our expectations. Variability in individual bands is expected to be accompanied with higher χ_{red}^2 values. For non-variable objects with random noise, no correlation is expected between the different band observations; thus, the Stetson index should be close to zero, while in the case of the real correlated variability the index, should be positive. To derive the mean and standard deviation of the obtained distributions (\bar{D} , σ_D), we performed an iterative 3σ clipping process. Then the cutoff value was computed as $\bar{D} + 5\sigma_D$ (Figure 6).

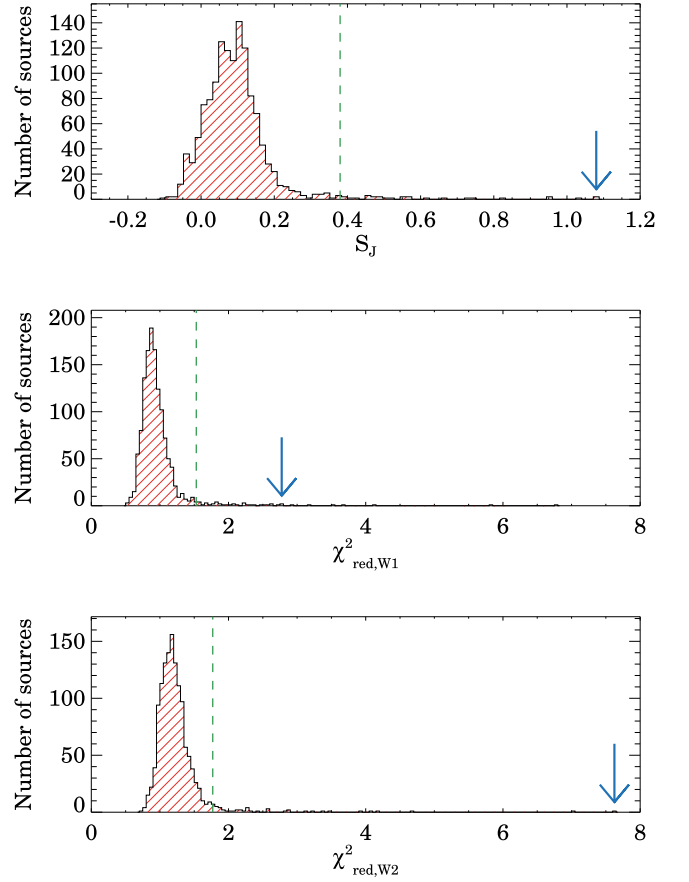


Figure 6. Histogram of the Stetson, $\chi_{\text{red,W1}}^2$, and $\chi_{\text{red,W2}}^2$ variability indices computed for WISE sources in the vicinity of TYC 5940. Blue arrows show index values obtained for TYC 5940, while vertical dashed green lines represent the derived cutoff values for the discrimination of non-variable/variable objects (see Section 5).

We found that the cutoff values differ from region to region: they range from 0.20 to 0.42 for the Stetson index, from 1.09 to 1.53 for the $\chi_{\text{red,W1}}^2$, and 1.74 to 2.58 for the $\chi_{\text{red,W2}}^2$ index. Interestingly, the means of the S_J distributions were found to be larger than zero (0.08–0.1) in all cases. This is in line with the result of Secret & Satyapal (2020), who, examining the mid-IR variability of dwarf galaxies, found that the distribution of Pearson correlation coefficients between WISE W1 and W2 band photometry follows a normal distribution that is slightly shifted toward positive values (with a mean of 0.06 and a standard deviation of 0.09). Table 5 lists the obtained variability indices and the relevant critical cutoff values; the latter ones are in brackets. We identified four objects—TYC 8105, TYC 5940, TYC 4209, and TYC 4479—that show significant variability. While the variation of TYC 8105 is limited to the W2 band, the other three systems exhibit flux changes in both WISE bands in a correlated way. The light curves of TYC 4515 and TYC 4946 display no significant variability. Repeating the above procedure using only data points obtained in the NEOWISE Reactivation phase would not change our conclusions on the variability of the targets (see Table 5).

We also examined whether or not the W1 – W2 color index of our targets showed any significant variations during the WISE observations. By calculating the $\chi_{\text{red,W1-W2}}^2$ values for our targets and for their comparison samples, and then using

Table 5
Variability Indices

Name	$\chi_{\text{red,W1}}$	$\chi_{\text{red,W2}}$	S_J	$\chi_{\text{red,W1-W2}}$
AllWISE + NEOWISE Reactivation data				
TYC 4515	0.99 (1.47)	1.76 (1.83)	0.21 (0.36)	1.08 (1.48)
TYC 5940	2.78 (1.53)	7.61 (1.93)	1.08 (0.38)	2.15 (1.55)
TYC 8105	1.25 (1.45)	2.51 (1.82)	0.20 (0.32)	1.48 (1.49)
TYC 4946	1.06 (1.48)	1.69 (2.58)	0.31 (0.42)	0.98 (1.72)
TYC 4209	19.18 (1.09)	105.20 (1.74)	5.72 (0.20)	14.52 (1.19)
TYC 4479	2.37 (1.44)	8.96 (2.21)	1.08 (0.37)	2.10 (1.60)
NEOWISE Reactivation only				
TYC 4515	0.86 (1.44)	1.66 (1.98)	0.27 (0.40)	0.88 (1.49)
TYC 5940	2.98 (1.49)	7.86 (2.01)	1.34 (0.40)	1.82 (1.56)
TYC 8105	1.19 (1.30)	1.99 (1.77)	0.24 (0.32)	1.19 (1.36)
TYC 4946	1.01 (1.37)	1.50 (2.34)	0.25 (0.41)	0.92 (1.61)
TYC 4209	20.46 (0.97)	113.04 (1.59)	6.05 (0.19)	15.56 (1.09)
TYC 4479	2.66 (1.35)	10.66 (1.93)	1.34 (0.36)	2.32 (1.48)

the above technique to set the thresholds, we found that the W1 – W2 colors of TYC 5940, TYC 4209, and TYC 4479 changed significantly between 2010 and 2019.

Figure 7 shows how the disk fluxes in the W1 and W2 bands—computed as the difference of the measured single-exposure photometry and the photospheric flux densities—of our targets changed between 2010 and 2019. In addition to the individual data points, their averages in each observing window (seasonal averages) were also plotted. In the course of averaging, an iterative sigma-clipping algorithm was utilized where the clipping was set to $3\times$ the standard deviation. Formal uncertainties were computed from the dispersion of data points involved in the averaging. Ratios of the W1 and W2 band disk fluxes as well as the corresponding color temperatures were also derived and plotted in separate panels.

The four variable objects are displayed in the first four panels of Figure 7. TYC 5940 exhibited significant variability in both WISE bands. Following an initial drop, in 2014, the object started brightening, and the disk flux increased by 78% in W1 and by 54% in W2 over 6 yr. TYC 8105 displayed less pronounced variations, with no long-term trend in the flux changes. According to our analysis, only the W2 band variability is formally significant, with a peak-to-peak amplitude of about 34%. The disk of TYC 4209 showed very prominent flux changes. After an intermediate flux level in 2010, its flux considerably dropped by 2014, which was followed by a dramatic brightening on a timescale of about 1 yr. At 3.4 and 4.6 μm , the disk became brighter by about 56% and 64%, respectively. Over the next 1 yr, the disk flux levels remained nearly constant, but after that, a significant fading started. By late 2017, the disk reached the flux level just preceding the brightening phase in 2014. The light curve between 2014 and 2017 was rather symmetric; the pace of rising and fading was roughly similar. In 2018, the disk started brightening again. TYC 4479 was constant between 2010 and 2015. In early 2016, an abrupt flux rise by a factor of two occurred in less than 6 months. The peak was immediately followed by an exponential-like fading. By 2019, the source returned to its normal flux level; thus, this asymmetric brightening event lasted for about 2.5 yr. The last WISE observation in 2019 August showed a higher flux level again. TYC 4515 and TYC 4946 exhibited no variability complying with the criteria of formal significance in our analysis. Nevertheless, the light curves of TYC 4946 suggest a wavelike pattern between 2014 and 2019, repeated in both the W1 and W2 bands.

5.2. Optical Variability of the Host Stars

In the calculation of IR excesses, we assumed that the host stars did not exhibit variability trends on the timescales of our WISE light curves in Figure 7. To evaluate this assumption and to exclude that the observed mid-IR flux changes could be driven by stellar variations, we examined the long-term optical light curves of the host stars of the four variable objects. The data were taken from the ASAS-SN survey (Shappee et al. 2014; Kochanek et al. 2017), which provides V-band photometry for the whole sky with a cadence of $\sim 2\text{--}3$ days. These measurements allowed us to investigate the optical properties over only a part of the NEOWISE Reactivation mission (Figure 7). However, they are still relevant since the specific disks showed significant changes in mid-IR wavelengths during this period as well.

Our analysis showed that all monitored stars were stable; their light curves were flat with rms noise < 0.02 mag. In the same time intervals, TYC 5940, TYC 4209, and TYC 4479 displayed peak-to-peak variations of 0.14, 0.39, and 0.17 mag, respectively, in the W2 band averaged photometry, which cannot be explained with variable stellar radiation. TYC 8105 shows a more modest change in the W2 band with a peak-to-peak change of 0.07 mag during the NEOWISE Reactivation mission. Based on TESS data (Appendix B), within our sample, this star exhibits the largest rotational modulation. However, even in this case, the amplitude is only 0.019 mag. Moreover, the length of the WISE observing windows are between 1.9 and 7.3 days for this object; thus, our averaging process within the windows mostly cancels the effect of the rotational variability, which has a period of ~ 5 days. A further indication that the observed W2 band change is associated with the disk is that the measured peak-to-peak change in the same time period in the W1 band—where the disk’s contribution is negligible—was only 0.022 mag.

5.3. Exploring the Hourly/Daily Variations

To examine disk flux variations on shorter hourly/daily timescales, we turn to WISE single exposures performed within a specific observational window. The length of individual data sets in these windows depends on the target’s sky position. Due to its high ecliptic latitude of $\sim 87^\circ$, TYC 4209 was observed for 17–34 days at a time. The other five targets have typical coverages shorter than a week. To identify objects showing significant variability on these shorter timescales, we used the same strategy as we described in Section 5.1, i.e., the variability indices (S_J and χ_{red}^2 values) computed for our target were compared to those of nearby similarly bright sources that are supposed to be mostly non-variable.

In the W1 and W2 bands, where photometry was available for all epochs, we found significant variability only in one source, TYC 4209, in two observational windows (2015 October 19–November 5; 2017 April 8–May 11; marked in Figure 7) in both bands. Note that this source has by far the broadest observing window in our sample. The WISE light curves are displayed in Figure 8, showing both the individual single exposures and 10-point binned values. In both windows, a fading trend can be recognized. The observed trends were characterized by fitting a straight line to the binned data considering their error bars. These yielded slopes of $b_{W1} = -53 \pm 11 \text{ mJy yr}^{-1}$ and $b_{W2} = -75 \pm 11 \text{ mJy yr}^{-1}$ in the first window and $b_{W1} = -17 \pm 4 \text{ mJy yr}^{-1}$ and $b_{W2} = -23 \pm 4 \text{ mJy yr}^{-1}$ in the second window. All obtained

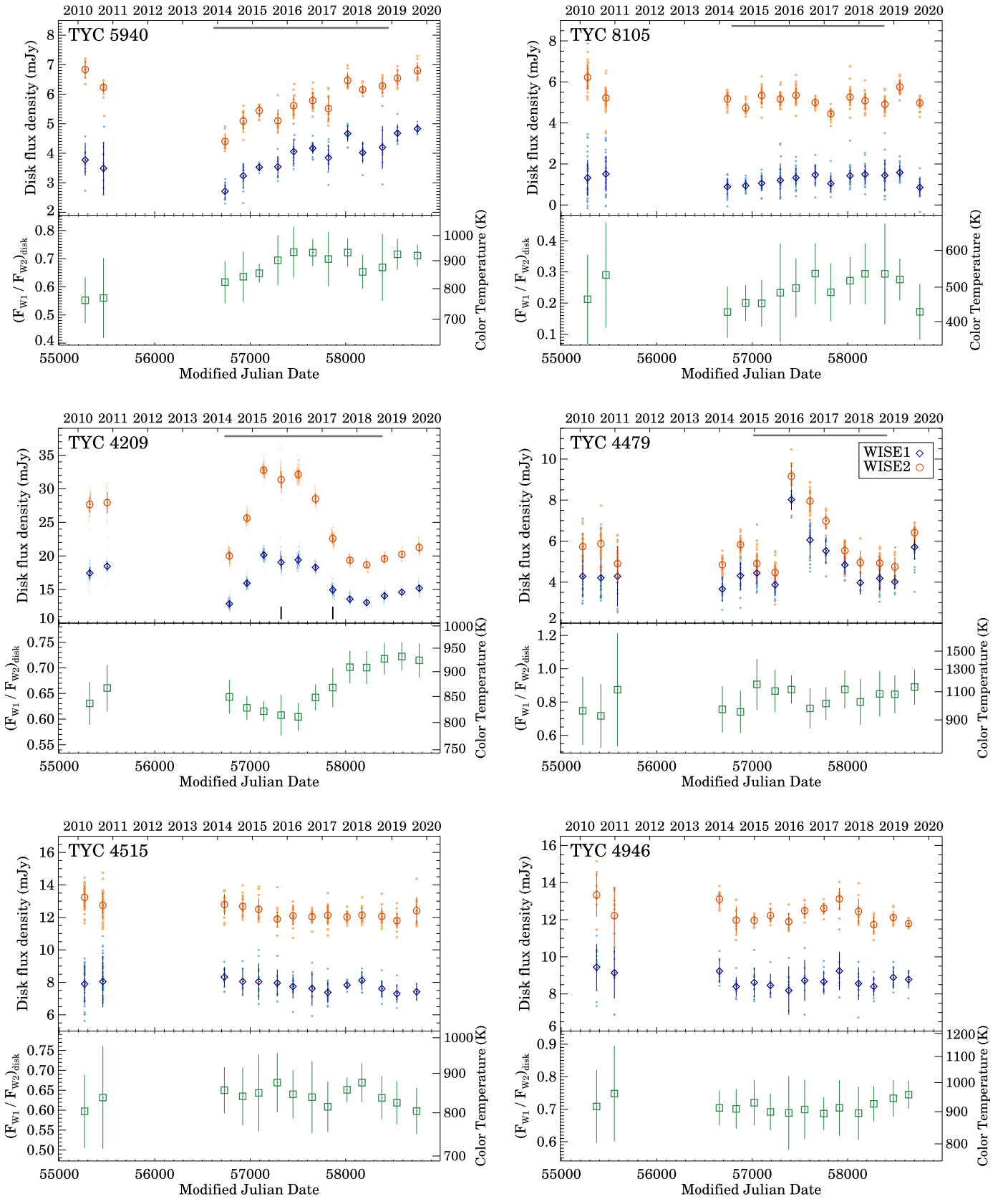


Figure 7. WISE W1 (3.4 μm) and W2 (4.6 μm) band disk fluxes (the measured excess emissions) for our targets between 2010 and 2019. Small dots show single-exposure data points, while larger symbols with error bars denote the seasonal averages. Horizontal gray lines show the time ranges of available ASAS-SN photometric observations (Section 5.2). Small vertical lines in the plot of TYC 4209 mark those observational windows in which significant daily disk flux changes have been detected (Section 5.3). Ratios of W1 to W2 band seasonal averages are also shown (bottom panels) together with the corresponding color temperatures.

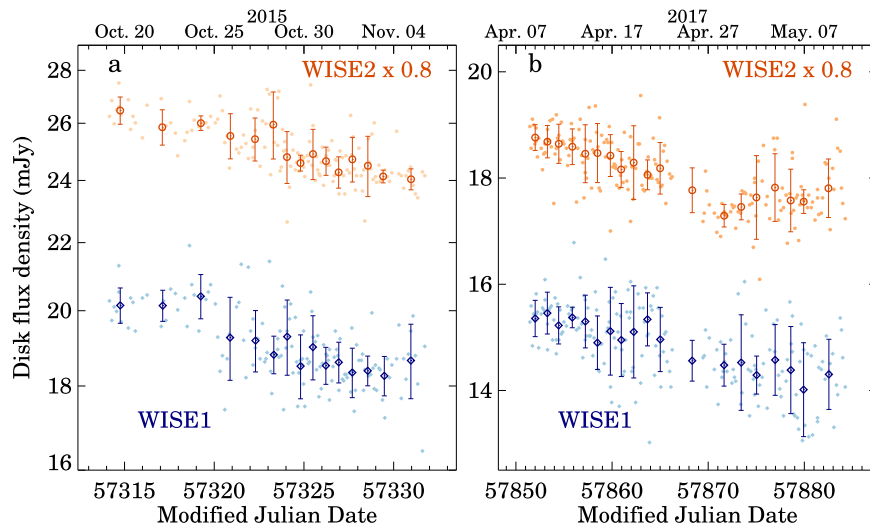


Figure 8. WISE W1/W2 band disk fluxes of TYC 4209 in the observational windows when significant flux changes were detected (Section 5.3). For better visualization, the W2 light curve was scaled by 0.8.

slopes are significantly different from zero. We compared these slopes with the long-term flux changes in Figure 7. In the first window, our result is consistent with the fading since the previous window, but its pace is much higher. Extrapolating the rapid fading would result in the disappearance of the excess on a timescale of ~ 0.5 yr. In contrast to this, the source became brighter by the next window ~ 6 months later. In the second window, the observed trend qualitatively matches the long-term fading behavior; however, the fading rate is faster. Similar few-weeks-long rapid variations are seen in Spitzer light curves of other EDDs (ID 8, P 1121) of better sampling (Su et al. 2019b). In those objects, the quasiperiodic changes were found and interpreted as orbital evolution of an optically thick dust cloud (Su et al. 2019b).

In the W3/W4 bands, our data are limited to one to two observing windows in 2010–2011. Using the same strategy as above, we found no significant daily variability in any of the sources.

5.4. Search for Decadal Changes

For five objects, additional IR photometry is available from different space missions (Table 4). In those four cases where IRAS measurements also exist, the data cover ~ 30 yr. These additional data allow us to check for long-term variability. Figure 5 shows the data points, together with the WISE photometry and the models fitted to the WISE data (Section 4.3). In most cases, the additional data match the model curves well. In TYC 4515 and TYC 5940, the IRAS $12\ \mu\text{m}$ data points exceed the models; however, even in these cases, the significance of the excess remains below 3σ . Moreover, in TYC 5940, the $12\ \mu\text{m}$ excess might be contaminated by a nearby source (Section 4.2). Thus, the available observations do not support any long-term IR variability exceeding the formal uncertainties in our sample.

6. Discussion

6.1. Steady-state or Transient Dust Production?

As a first step in analyzing the nature and origin of the observed abundant warm debris material around our targets, we examined whether it could be produced in a steady-state grind

down of an in situ planetesimal belt, a massive exo-solar analog of our solar system’s asteroid belt. If located close to the star, the evolution of such inner planetesimal belts would be very rapid due to the short collisional timescale. Based on the analytical steady-state evolutionary model of Wyatt et al. (2007), at any given age, there is a maximum possible fractional luminosity ($f_{d,\text{max}}$) of a debris ring. Following Wyatt et al. (2007), we adopted a belt width of $dr = 0.5r$, a maximum asteroid size of 2000 km, typical planetesimal strength of $Q_D^* = 200\ \text{J kg}^{-1}$, and planetesimal eccentricity of 0.05, which resulted in

$$f_{d,\text{max}} = 1.6 \times 10^{-4} \left(\frac{R_{\text{disk}}}{1\ \text{au}} \right)^{7/3} \left(\frac{M_*}{M_\odot} \right)^{-5/6} \times \left(\frac{L_*}{L_\odot} \right)^{-1/2} \left(\frac{t}{\text{Myr}} \right)^{-1}. \quad (4)$$

Wyatt et al. (2007) argued that, even by considering the uncertainties in their model, debris rings with $f_d/f_{d,\text{max}}$ ratios higher than 1000 could not be produced through steady-state processes, but should be linked to some transient event instead. For computing $f_{d,\text{max}}$, stellar and disk parameters were taken from Table 1. By assuming that the collisional cascade started early, for t we adopted the age of the systems (Table 1). For our targets, the ratios of the measured fractional luminosities to the theoretical maxima (Table 1) range between $\sim 8 \times 10^4$ and 2.6×10^6 . We note, however, that $f_{d,\text{max}}$ strongly depends on the disk radius, which is not reliably known. In Section 4.3 we used a simple blackbody model, which can lead to an underestimation of the disk radii. Based on debris disks spatially resolved by the Herschel Space Observatory, in systems with sunlike host stars, the ratios of the true disk radii to the blackbody radii are < 5 (Figure 4(b) in Pawellek et al. 2014). Entering $5 \times$ larger radius values into the equation results in $\sim 43 \times$ higher $f_{d,\text{max}}$ values. However, even this way, we still get $f_d/f_{d,\text{max}} > 1800$ for all sources, implying they are probably experiencing a transient phase.

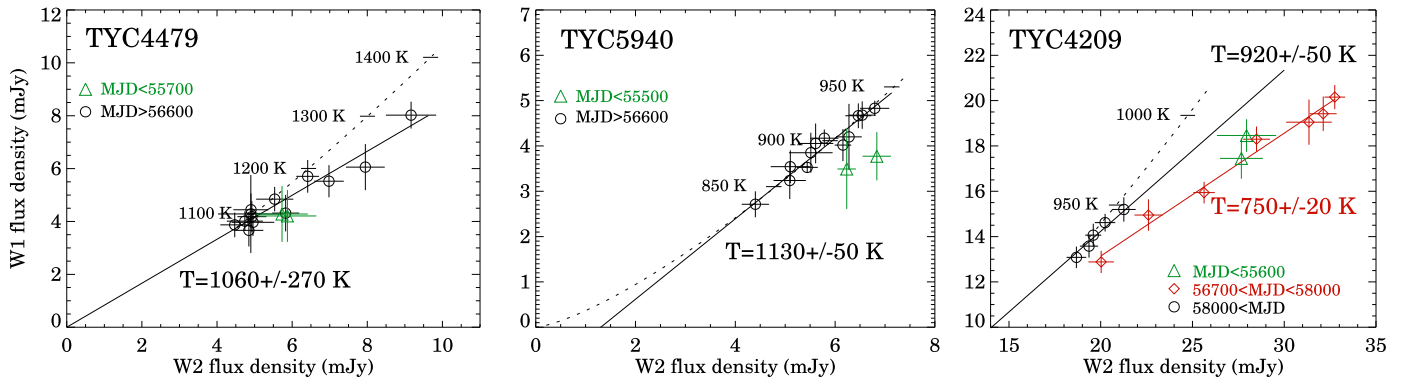


Figure 9. Correlation of the WISE 3.4 and 4.6 μm flux densities using the seasonal averages of three EDD formally exhibiting variability (Section 5, Figure 7). Solid lines represent models of constant temperature with varying dust emitting surface, while dotted lines denote the emission of a dust population of increasing temperature with constant emitting surface.

6.2. The Origin of Disk Variability

Figure 7 shows that in most objects, parallel to the detected mid-IR flux changes, the color temperature derived from the ratio of the 3.4 and 4.6 μm fluxes was also variable. In order to identify the physical processes behind these variations, we correlated the W1 and W2 multi-epoch fluxes, by plotting the seasonal averages in Figure 9. The photometric point distributions were then confronted with the predictions of two simple models: the first one assumes that the temperature of the circumstellar dust grains can change in time, while the second one keeps the temperatures constant but varies the total emitting dust surface area. Variability caused by the latter process would appear in Figure 9 as a straight line whose slope is related to the invariable temperature, while a temperature rise in the first model would outline a curve starting from the origin.

The distribution of the WISE data points of TYC 4479 in Figure 9 (left) is consistent with a line crossing the origin within the formal fit uncertainties. The derived 3.4/4.6 μm color temperature is 1060 K. The points are inconsistent with a model where the temperature of the dust grains would increase above 1060 K, because it would have made the resulting emission bluer, which is not seen in the data (dotted curve). Thus, for the observed variability of TYC 4479, the most plausible model is the change of the effective surface area. It may be caused by the production of fresh dust, but it may also be due to geometrical rearrangement of the ring structure, which would temporarily decrease the dust column density and make the IR emission less optically thick. The minimum emitting area in the faintest state (assuming optically thin blackbody radiation) was 0.00023 au^2 , while at the brightness peak, it rose to 0.00046 au^2 , doubling the dust surface within a few months. Note that if the dust is partly optically thick, then these estimates are lower limits. Taking into account the luminosity of the star (Table 1), the blackbody radius of the 1060 K dust is ≈ 0.06 au.

The IR time variability of TYC 5940 (Figure 9, middle) can be explained by both of our simple models. The data points form a straight line, which, however, does not reach the origin. The nonzero intercept is significant at the 5σ level. The data are also compatible within the measurement uncertainties with a model of increasing dust temperature (dotted curve). Thus, one possible interpretation is that we see a dust population, located at 0.06 au from the star at an equilibrium temperature of 1130 K, which changed its emitting area between 0.00034 and 0.0006 au^2 over the observed period. The nonzero intercept

may point to the existence of a colder dust population (probably at larger stellocentric radius), whose thermal emission at 3.4 μm is still negligible, but at 4.6 μm becomes detectable. An equally plausible model is, however, that the area of the dust ring remained constant while its temperature increased from ≈ 850 to ≈ 950 K. The origin of the energy needed for the extra heating is unlikely to arrive from the star (in Section 5.2 we argued for a low level of stellar variability), raising the question about the heat source.

The most complex case of variability is TYC 4209. This source exhibited a broadly symmetric brightness peak in 2014–2017 (Section 5), followed by smaller-scale variations. The two periods show different color temperature behaviors (Figure 7). In order to examine the physical reasons of variability separately, we plotted in Figure 9 (right) the data points of the two periods with different symbols. The flux changes after the brightness peak (MJD > 58,000, black circle) can be modeled with a straight line reaching the origin within the uncertainties of the fit parameters. This would imply an increasing emitting surface of a $T = 920$ K dust population, located at 0.11 au from the star, from 0.0041 to 0.0047 au^2 . The observations are also marginally consistent with the warming up of this dust ring from ≈ 920 K to ≈ 950 K. The 2014–2017 brightness maximum, however, seems to be intrinsically different from the previous process. It is clearly inconsistent with any variable dust temperature model. Since its emission appears as an addition to the flux of the 920 K dust ring, we suggest that we have witnessed the appearance and subsequent disappearance of a cloud of fresh dust at a temperature of $T \approx 750$ K, with an emitting area of 0.006 au^2 . This temperature corresponds to a radius of 0.17 au, significantly farther than the first ring. Outside the most opaque core of the $T = 920$ K ring, the optical depth of the circumstellar dust is probably below unity; thus, a geometrical rearrangement of the dust at $r = 0.17$ au would be an unlikely cause of the emission peak, leaving the formation of new dust via collisions as the most likely physical picture.

The last, formally variable object, TYC 8105, could not be analyzed with these techniques because of the large error bars and the limited dynamic range of the data points.

The temperatures yielded above are higher than the characteristic dust temperatures derived from the blackbody fit to the 3.4–22 μm band IR excess (Section 4.3). This may indicate that these disks present a range of dust temperatures and their dust material is distributed over a broad radial range.

6.3. The Nature of the EDD Phenomenon

In addition to the six systems studied in this paper, 11 additional EDDs are claimed in the literature (Appendix C). Apart from HD 113766 and HD 145263, where the host stars are F2-type dwarfs, all of these disks surround solar-type (F5-K3 type) stars. The nature of two of these additional disks is still debated. RZ Psc was found to exhibit a weak accretion signature, suggesting that the disk may be of primordial nature rather than EDD (Potravnov et al. 2017, 2019). Concerning HD 166191, Kennedy & Wyatt (2014) raised the possibility that it is not a secondary disk but a primordial transition disk. However, based on recent millimeter continuum and line observations of this system, both the measured low CO gas mass and the low gas-to-dust mass ratio are more consistent with a debris disk nature (Garcia & Hughes 2019). Despite their debated classification, both objects are included in our analysis. The case of TYC 8241-2652-1 is quite special: before 2010, this young K-type star hosted a warm (~ 450 K), unusually dust-rich disk, whose mid-IR luminosity then decayed significantly over less than 2 yr, leaving behind a colder (< 200 K), tenuous disk (Melis et al. 2012). Recent observations indicated that the disk has remained depleted (Günther et al. 2017). Table C1 shows the parameters valid before 2009, which were consistent with an EDD. In the following, we will consider the whole sample of EDDs, including all sources proposed in the literature and the ones in this paper, to examine their mid-IR variability, age distribution, and the multiplicity of the host stars. We will also assess what these characteristics indicate about the nature of EDDs.

6.3.1. Mid-infrared Variability of EDDs

Many of the previously known 11 EDDs were targets of multiyear photometric monitoring campaigns performed by Spitzer at 3.6 and 4.5 μm . These studies revealed significant variability on monthly to yearly timescales—in some cases with very complex variability patterns—in seven of them: HD 15407, HD 23514, BD+20 307, ID 8, P 1121, HD 113766, and HD 166191 (Meng et al. 2014, 2015; Su et al. 2019b, 2019a, 2020). HD 145263 was found to show no significant disk variations based on its Spitzer observations in 2013 (Meng et al. 2015).

In addition to Spitzer data, WISE measurements are available for all 11 sources, allowing us to study their mid-IR flux changes over the AllWISE and NEOWISE Reactivation mission phases between 2010 and 2019. The steps and results of this analysis are presented in Appendix C. The three brightest sources, HD 15407, HD 113766, and HD 166191, are saturated in both bands, preventing us from drawing reliable conclusions regarding their variability (we note that their Spitzer data point to substantial variability). A similar issue affects the W1 photometry of HD 145263 and BD+20 307. The W2 light curves of the latter two objects displayed no significant variability over the given period.

As Figure C1 demonstrates, for HD 23514, ID 8, and P 1121, WISE measurements confirm the previous Spitzer-based results, proving that these disks exhibit well-detected flux changes between 3 and 5 μm . While during the Spitzer observations in 2013, the disk of HD 23514 showed a fading trend, its NEOWISE Reactivation measurements indicate a slow brightening since 2014. For ID 8, WISE measurements from 2018–2019 complement the previous Spitzer data, showing that the disk continues to display significant changes. The WISE light curves of RZ Psc (see

also those in Kennedy et al. 2017) and V488 Per show evidence of strong variability in both the W1 and W2 bands. It is noteworthy that between 2019 January and August, the disk of V488 Per became ~ 7 and ~ 4 times brighter at 3.6 and 4.5 μm , respectively, and it is now brighter at these wavelengths than ever observed before. This is the largest increase we have seen in any EDDs at any given six month interval. Although the WISE fluxes of TYC 8241-2652-1 did not show significant changes between 2010 and 2019, before this period, its disk underwent a dramatic fading (Melis et al. 2012).

Thus, in the case of the previously known EDDs, there were significant flux changes in 10 out of the 11 sources, while in our sample, four disks out of the six proved to be variable. In summary, 14 out of the 17 EDDs have shown significant variability in the wavelength range of 3–5 μm over the past roughly 10 yr. Flux changes can be observed even in the oldest EDD systems; both TYC 4209 and TYC 4479 exhibit substantial variations. These results indicate that the variability phenomenon is an inherent characteristic of EDDs.

Although the light curves of EDDs show a large variety in their shape, some of them exhibit similar patterns. Between 2015 and 2019, the disks of HD 23514 (Figure C1) and TYC 5940 (Figure 7) showed analogous slowly rising trends both at 3.4 and 4.6 μm . The light curves of ID 8 display a wavy pattern (Figure C1); the successive brightening and fading periods occur on a yearly timescale and probably represent the aftermath of violent impact events (Su et al. 2019b). As Figure 7 demonstrates, the WISE data of TYC 4209 and TYC 4479 show similar ripples; although in these cases, in contrast to ID 8, the rising phase is steeper than the declining one. These bumps might also be attributed to significant dust releasing events. In the case of ID 8, Su et al. (2019b) found that the observed 4.5 μm flux change associated with the decay in 2013 corresponds to a total cross-sectional change of 0.0021 au^2 . Based on WISE data, the inferred cross-sectional change at TYC 4209 is $\sim 3\times$ higher, while at TYC 4479, it is $\sim 9\times$ lower (Section 6.2).

6.3.2. Wide-separation Companions

Examining a smaller EDD sample available at that time (five disks around 30–100 Myr old solar-type stars), Zuckerman (2015) suggested that these disks are situated preferentially in wide binaries. Considering that five of our disks are also found in similar systems, it is worth looking again at this possible relationship using the now much larger sample. As mentioned above, out of the previously known 11 EDDs, nine have solar-type (F5-K3 type) host stars, from which (so far) five are proven multiples. BD+20 307 is composed of two late-F-type main-sequence stars in a close orbit ($P \sim 3.4$ days; Weinberger 2008; Zuckerman et al. 2008). Using Gaia DR2 astrometric data, Hartman & Lépine (2020) identified a new common proper motion companion of this star at a projected separation of 8''4 (980 au). This wide companion is classified as a white dwarf candidate with a mass of 0.48–0.58 M_{\odot} (depending on whether a pure-He or pure-H atmosphere is supposed; Gentile Fusillo et al. 2019). Recently, Kennedy et al. (2020) reported the discovery of a low-mass companion of RZ Psc at a projected separation of 23 au. The other three stars, HD 15407, HD 23514, and V488 Per, are all reported to have wide-orbit companions, the projected separations of which are $\rho_p = 1050, 365,$ and 12,300 au, respectively (Melis et al. 2010; Rodriguez et al. 2012; Zuckerman 2015). V488 Per

possibly hosts a second low-mass companion at $\rho_p \sim 12,000$ au (Zuckerman 2015).

Using the method and requirements we described in Section 3.3, we searched the Gaia EDR3 catalog for previously unknown common proper motion pairs of these nine stars. This confirmed the findings of Hartman & Lépine (2020) for BD +20 307 and yielded new faint candidate pairs for three more stars, V488 Per (five candidates, all with $\rho_p > 0.39$ pc), HD 23514 (one candidate, $\rho_p = 0.41$ pc), and P 1121 (one candidate, $\rho_p = 0.74$ pc). However, all of these stars are members of young open clusters (V488 Per: α Per open cluster, HD 23514: Pleiades, P 1121: NGC 2422). By studying wide binary systems in the α Per, Pleiades, and Praesepe open clusters, Deacon & Kraus (2020) demonstrated that at projected separations >3000 au, it is difficult to separate true binaries and unrelated cluster members. Although it cannot be completely ruled out that some of the revealed candidates are true binaries, the separations suggest that they instead fall into the latter category. Therefore, these were not taken into account in our further analysis. Based on the same arguments, Deacon & Kraus (2020) do not list V488 Per as a probable wide binary, because, due to their large separations, the previously reported companions (at $\rho_p \sim 12,000$ au, see above) could also be unrelated cluster members. Therefore, in the following, we do not consider this system as a justified binary.

Putting it all together with our results, out of the 15 EDDs with solar-type hosts, there are eight systems ($53.3^{+11.6}_{-12.4}\%$) with wide-separation (365–6010 au) companions. Remarkably, all of them are older than 100 Myr. Thus, at ages <100 Myr (five EDDs out of the 15) no wide binaries were found, while at ages >100 Myr (10 EDDs), the multiplicity fraction is $80^{+7.1}_{-17.2}\%$. Considering the small sample, the uncertainties were derived by adopting a binomial distribution (Burgasser et al. 2003). For the majority of the EDD systems, the information about wide companions is based on data from the Gaia EDR3 catalog. There are possible limitations of this approach. By testing the small-scale completeness of this data release based on source-pair distances in a small dense field near the Galactic plane, Fabricius et al. (2020) claimed that the completeness falls rapidly at separations less than $0''.7$. This value corresponds to ~ 300 au at P 1121, which is the farthest object in the sample. Of course the detection sensitivity of possible companions depends not only on the angular separation but on the brightness ratio of the pair as well (Brandeker & Cataldi 2019). Even in pairs with large angular separations, it is possible that the companion is too faint to have a proper astrometric solution in the current Gaia data release. Future observations with ground-based high-contrast facilities and with Gaia have the potential to reveal additional fainter and less-wide companions in these systems.

In order to put these results into context, we need to know the incidence of similar binaries among solar-type stars. Based on the log-normal distribution derived by Raghavan et al. (2010) for separations of companions around F6–K3 type main-sequence stars, about 13% of such dwarfs have at least one companion at separations between 300 au and 1 pc. This fraction is $\sim 4\times$ lower than what we observe among solar-type EDD stars. By applying a binomial test (using the R statistical programming language’s `binom.test` function), we obtain a probability of 2.3×10^{-4} for the null hypothesis that the fraction of wide binaries in the EDD sample is equal to or lower than in the comparison sample. If we consider only

objects older than 100 Myr from the EDD sample, the contrast is even stronger: the observed wide companion fraction in that subsample is $\sim 6\times$ higher than among normal solar-type stars. In this case, a binomial test yields a probability of 3×10^{-6} for the above-mentioned null hypothesis, i.e., it could be rejected with high statistical reliability.

However, while most EDD host stars are likely younger than 300 Myr, the comparison sample predominantly contains older stars. This must be taken into account in the comparison, since the frequency of weakly bound wide binaries can decline with time as a result of gravitational influence due to encounters with other stars and giant molecular clouds (Weinberg et al. 1987). In a recent survey of the 10 Myr old Upper Scorpius association, Tokovinin & Briceño (2020) found that the fraction of $100\text{--}10^4$ au pairs with solar-type primaries resembles that of stars in the field. By scrutinizing members of nearby young moving groups (5–100 Myr old), Elliott et al. (2015) also claimed that the multiplicity frequency of solar-type stars in the separation range of 10–1000 au is similar to that in the field star sample compiled by Raghavan et al. (2010). Deacon & Kraus (2020) confirmed these results by reaching the conclusion that the fraction of pairs with separations of >300 au among FGK-type stars belonging to nearby 10–200 Myr old young moving groups and to the ~ 125 Myr old Pisces-Eridanus stream shows no significant excess over that of similar-type older field stars. In the same study, they showed that compared to these low-density formation environments and field stars, there appears to be a deficit of wide (300–3000 au) binaries in open clusters. Actually, the α Per, Pleiades, and Praesepe clusters have an average binary fraction of 3% (with FGK-type primaries) in this projected separation range. We note that in the “old” (>100 Myr) EDD sample, the corresponding fraction is 6/10. Based on these results, there is no indication that the incidence of wide binaries would be significantly higher in younger samples, confirming that our previous comparisons with the field star sample do not require corrections. Our results thus imply that very-wide-orbit pairs are more common in EDD systems than in the normal stellar population.

6.3.3. Age Distribution and Disk Evolution

EDDs are thought to be produced in violent collisions occurring between planetary embryos during the final accumulation of terrestrial planets (Jackson & Wyatt 2012; Genda et al. 2015; Su et al. 2019b). If so, then by studying their age distribution, we can put observational constraints on the timeline of rocky planet formation around sunlike main-sequence stars. Figure 10 shows the ratios of the measured 4.5 or 4.6 μm flux densities to the predicted stellar photospheric fluxes as a function of ages for all 17 EDDs. Variability flux ranges, when applicable, are shown by the vertical dotted lines. For BD+20 307, HD 15407, and HD 113766, we used Spitzer 4.5 μm photometry taken from the literature (Meng et al. 2015; Su et al. 2019b). HD 166191 exhibited a strong brightening in 2019 (Su et al. 2019a), the corresponding individual Spitzer data points of which are presented in K. Su et al. (2021, in preparation). For the rest of the sample, WISE 4.6 μm data are plotted, where the minimum and maximum fluxes were taken from the light curves plotted in Figures 7 and C1. In the case of TYC 8241-2652-1, only the minimum flux was obtained in this way; the maximum flux at 4.6 μm was estimated from its disk model constructed by Melis et al. (2012) considering the IRAS

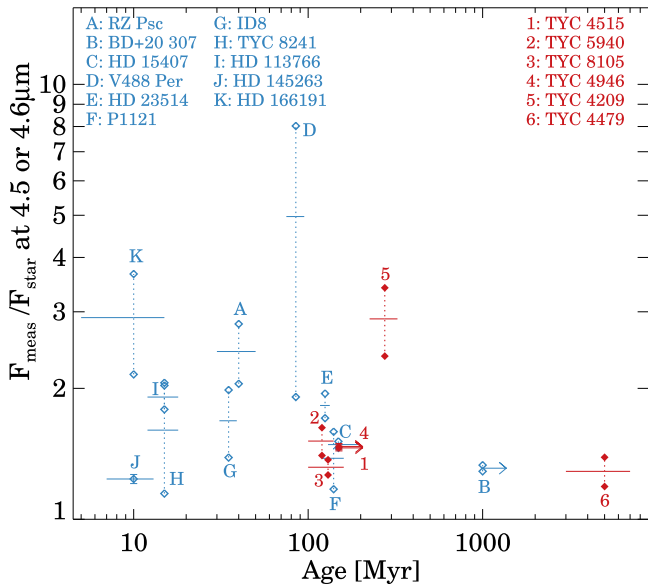


Figure 10. Ratios of the measured WISE2 band ($4.6\mu\text{m}$) flux densities to stellar photospheric fluxes as a function of age for extreme debris disks. Blue empty symbols show the 11 previously known objects, while red filled symbols denote our targets from Table 1. Variability ranges are shown by vertical dotted lines.

measurements of the source. For HD 145263, which is constant based on both Spitzer and WISE time-domain data, AllWISE W2 band photometry was utilized, after correcting for saturation by applying the method described in Cotten & Song (2016).

In our solar system, the era of giant impacts probably ended by a collision between the proto-Earth and another body that led to the formation of the Earth–Moon system (Canup & Asphaug 2001). Analyses of radioactive isotopes yield age estimates between 30 and 110 Myr for this event (Jacobsen 2005; Touboul et al. 2007; Halliday 2008; Kleine et al. 2009). Quintana et al. (2016) used N -body simulations to examine the formation of planets in the terrestrial zone of a sunlike star that harbors giant planets analogous to Jupiter and Saturn. Their initial disk included 26 Mars-sized planetary embryos and 260 smaller, approximately Moon-sized bodies. They found that most of the collisions took place in less than 100 Myr: in models where fragmentations were enabled, 90% of collisions occurred within the first 82 Myr, and 50% of them in the first 20 Myr. Nevertheless, based on the simulations, large collisions can happen even after hundreds of millions of years (up to 1 Gyr), although these are quite rare. Genda et al. (2015) reached a similar conclusion in their simulations without giant planets: the final giant impacts were found to occur at 73 ± 74 Myr. The age distribution of EDDs differs significantly from these results. Although most of the systems are probably younger than 500 Myr, and thus can even be the result of a similar major collision, the majority of them ($\sim 60\%$ of the sample) are older than 100 Myr, and at least three of them ($\sim 20\%$) have an age of >200 Myr. Thus if EDDs are associated with rocky planet formation, then our results, displayed in Figure 10, hint that the intensity of these processes—contrary to what solar system experienced and what is predicted by the simulations—does not decay significantly even after 100 Myr. Obviously, the simulations examined only a fraction of the possible parameter space. The presence of giant planets and their architecture, as well as the

mass and location of embryos/planetesimals in the terrestrial zone at the beginning of the giant impact era may have a serious influence on the timeline of planet formation (Quintana et al. 2016; Barclay et al. 2017). However, it is questionable whether all of these can cause such prolongation of rocky planet formation processes as suggested by our results.

6.3.4. Alternative Scenarios for the Formation of EDDs

Alternatively, it is possible that some other mechanism(s) can also produce EDDs, and this process is more typical in slightly older systems. When speculating on such mechanisms, we must consider that, based on the available observational characteristics, the older EDDs are quite similar to the younger ones. Though the average fractional luminosity of disks older than 100 Myr is somewhat lower than that of the younger objects, their characteristic dust temperatures are similar, and they display mid-IR variations with the same frequency and comparable amplitudes. A possible alternative mechanism should be able to explain these properties.

Single giant collision in an inner planetesimal belt—Although the formation of EDDs is certainly not explicable by the long-term steady-state collisional evolution of an in situ planetesimal belt (Section 6.1), individual giant impacts may happen in a collisionally depleted belt as well. However, considering that during the collisional evolution the number of large bodies, whose destruction can reproduce the observed dust quantity, is also decreasing, the probability of witnessing such an event falls off as $\propto t_{\text{age}}^{-2}$ (Wyatt et al. 2007). This is inconsistent with the observed age distribution. Actually, according to Wyatt et al. (2007), disks with high $f_d/f_{d,\text{max}}$ (Section 6.1), which cannot be the result of the steady-state evolution of a planetesimal belt, cannot be explained with such single giant collisions either.

Sublimation and disruption cometary bodies—Comets transported from an outer reservoir into the inner regions are also widely considered as possible sources of warm debris material (e.g., Wyatt et al. 2007; Morales et al. 2011; Bonsor et al. 2012; Ballering et al. 2017; Marino et al. 2017). Actually, in our solar system, the zodiacal dust particles dominantly stem from comets (Nesvorný et al. 2010; Rowan-Robinson & May 2013). Detections of non-photospheric, sometimes variable, absorption features toward several stars imply cometary activity in other systems as well (e.g., Beust et al. 1991; Kiefer et al. 2014; Welsh & Montgomery 2015; Iglesias et al. 2018; Rebollido et al. 2020). Due to the substantially longer collisional times, the depletion of cold outer planetesimal belts is much slower than that of inner Asteroid Belt analogs. Therefore, minor bodies originating from such reservoirs can supply dust in the inner zones even long after the local belt has largely been exhausted. These icy bodies can contribute to the production of warm dust in several ways. Dust grains can arise from the sublimation and disruption of comets, as well as from collisions of the inwardly scattered objects with each other and/or with inner rocky bodies.

Planetesimals can evolve into more eccentric orbits under the gravitational influence of planets or stellar companions, or because of a close stellar encounter. Investigation of scattering processes revealed that efficient, long-term inward transport of planetesimals from an outer belt requires a special architecture: the presence of a chain of closely spaced low-mass planets (Bonsor et al. 2012, 2014; Marino et al. 2018). As Faramaz et al. (2017) demonstrated, interactions between planetesimals and an outer eccentric planet can also drive a vast number of

icy bodies to highly eccentric orbits, which then can produce warm dust grains in the inner system on gigayear timescales. Transient events with a shorter timescale may also be of interest. A rearrangement of the planetary system following a dynamical instability—akin to the hypothesized late heavy bombardment scenario in our solar system (Tera et al. 1974; Booth et al. 2009; Bottke & Norman 2017)—can cause shorter-lived, significantly enhanced cometary activity. A companion or a star passing close by might also result in a transient spike in the warm dust production by initiating a comet shower from an outer planetesimal belt or from a reservoir analogous to the solar system’s Oort cloud.

In the following, we examine whether the cometary scenario can explain the peculiarly high dust content of EDDs. As a minimal EDD, we consider a 0.25 au wide debris belt that is located at 0.5 au around a Sun analog star ($L_* = 1 L_\odot$, $M_* = 1 M_\odot$) and has a fractional luminosity of 0.01. To estimate its mass-loss rate, we used Equation (29) from Wyatt et al. (2007) and obtained $\sim 0.17 M_\oplus \text{ Myr}^{-1}$. Supposing a dust-to-ice-mass ratio of 1 in the comets and that their material is converted to dust grains with a 100% efficiency, the sustenance of the above model EDD over 100 Myr would require the destruction of $34 M_\oplus$ of icy planetesimals in the inner zones. By simulating various multi-planet architectures, Marino et al. (2018) found that at most $\sim 7\%$ of planetesimals scattered from an outer belt via the planets reached the inner regions. Taking this maximum fraction, the long-term supply of the disk in a steady-state manner would require an unrealistically high total planetesimal mass of $\gtrsim 500 M_\oplus$ in the outer reservoir. This suggests that even in the cometary scenario, it is more likely that the observed phenomenon is related to a short-lived transient event rather than a continuous long-term comet flux.

Based on the cometary model developed by Marboeuf et al. (2016), we can make an estimate of how many active comets would be needed to provide the above-derived dust production rate. Using their Equations (17)–(19), we find that a comet with a radius of 1 km located 0.5 au from a star with $L_* = 1 L_\odot$ releases dust with a rate of $\sim 5300 \text{ kg s}^{-1}$. Roughly 6 million such active comets are needed to supply our minimum EDD. Supposing larger icy planetesimals with a radius of 100 km, i.e., with a size roughly corresponding to the largest Centaurs in the solar system, the required number would be ~ 600 . Since a large fraction of scattered icy bodies never reaches the snow line, and even those that do spend only a part of their orbital time within the line, the total number of comets involved in the process has to be much higher than this. However, this calculation only considers the dust production driven by the sublimation of icy bodies. According to Nesvorný et al. (2010), in the solar system, the spontaneous disruption of Jupiter family comets (JFCs) is the main source of the zodiacal dust. Moreover, the presence of a large number of comets in the terrestrial zone increases the chance of collisions with inner planets and other comets. Thus, it is entirely possible that in EDDs the latter two processes dominate the supply of dust and, therefore, far fewer active comets are sufficient to explain the observed excess.

Disruption of large comets and giant impacts is accompanied by rapid, vigorous dust release that can also explain the high-amplitude mid-IR changes seen in EDDs. For TYC 4479 and TYC 4209, the observed mid-IR brightening requires a minimum dust cross-sectional change of $2.3 \times 10^{-4} \text{ au}^2$ and $6.0 \times 10^{-3} \text{ au}^2$, respectively (Section 6.2). How large should a

disintegrating comet be to produce the necessary amount of dust? In the solar system, disruption of JFCs produces millimeter- to centimeter-sized particles that later collisionally grind down to smaller fragments (Nesvorný et al. 2010). Assuming that the dust material of the comet (half of its total mass) turns into $0.5 \mu\text{m}$ – 1 mm grains in a power-law size distribution with an index of -3.5 and taking an dust-to-ice density ratio of 3, the reproduction of the derived cross sections needs the disruption of a planetesimal with a radius of $\sim 50 \text{ km}$ and $\sim 160 \text{ km}$ for TYC 4479 and TYC 4209, respectively. These sizes should be considered as lower limits since (1) the disruption may not be so efficient, (2) the average size of the emerging particles is probably underestimated, and (3) the estimated cross-sectional values are also lower limits (Section 6.2). We note that collisions between objects of the sizes computed above can also provide a good explanation for the observed flux changes (e.g., Su et al. 2019b).

The possible role of dynamical instabilities—As mentioned earlier, the temporarily enhanced comet activity could be due to a dynamical instability of the planetary system. On their changed orbit, planets can perturb neighboring planetesimal populations, leading to their excited eccentricities, causing an increased flux of infalling icy planetesimals in the terrestrial regions. Although the aftermath of such instabilities can last for up to a few 10 Myr, the enhanced level of exozodiacal dust typically decays on a timescale of a few million years (Bonsor et al. 2013). Figure 2 of Bonsor et al. (2013) suggests that even within this period, there could be a shorter peak in the comet flux. By the end of such an instability event, the outer planetesimal belt can be substantially depleted (Booth et al. 2009). The mass inflow of comets might be sufficiently high to produce an EDD. However, although the NICE model of the solar system demonstrates that a dynamical instability can be delayed to 100 million yr (Gomes et al. 2005), Bonsor et al. (2013) claims that such instabilities are more frequent in younger systems (typically $< 10 \text{ Myr}$). Thus, this mechanism, similarly to the rocky planet formation scenario, is unable to offer a solution for the observed age distribution, although it may explain the origin of some individual systems.

The possible influence of wide companions—Intriguingly, we found that very-wide-orbit pairs are more common in EDD systems than in the normal stellar population (Section 6.3.2). This is particularly true for EDDs older than 100 Myr: out of the 10 objects, eight are located in wide binaries. This raises the question of whether or not the two phenomena may be physically connected. One possibility is that, as a consequence of impulses from passing stars and torques from the Galactic tide, orbits of very wide ($a \gtrsim 1000 \text{ au}$) binary stars can become very eccentric after a time (Jiang & Tremaine 2010; Kaib et al. 2013; Bonsor & Veras 2015). Due to the decreasing pericenter radius, the companion can launch a comet shower when approaching the outer population of planetesimals. Indeed, the 365–6000 au projected separations found in the sample are comparable to the size of the scattered disk or the Oort cloud in the solar system. This mechanism is able to produce an excess population of long-period comets. A favorable aspect of this model is that the orbital change of the companion requires time; thus, this process could occur much later than 100 Myr, too. However, this hypothesis has several drawbacks. Long-period comets are on very eccentric orbits and spend only a small fraction of their revolution within the snow line; thus, the dust production is limited. Moreover, simulations of perturbations

caused by a companion or a stellar flyby predict a comet flux increase of at most a few orders of magnitude, which means a few tens of such comets per year (Davis et al. 1984; Berski & Dybczyński 2016)—far below the required level. Therefore, this scenario alone probably cannot explain the observed dust contents.

A companion with an initial inclination (i_c) between $\sim 39^\circ$ and $\sim 141^\circ$ with respect to the orbital plane of a third body (e.g., a planetesimal or a planet) can cause oscillations in the eccentricity and inclination of this body via the Kozai–Lidov (KL) mechanism (Naoz 2016). The timescale of this effect depends on the mass (m_c), orbital period (P_c), and eccentricity (e_c) of the companion, the total mass of the primary, the perturber, and the disk ($m_{\text{tot}} = m_{\text{pr}} + m_c + m_{\text{disk}}$), and the orbital period of the disk’s particles (P) (Nesvold et al. 2016):

$$t_{\text{KL}} \sim \frac{m_{\text{tot}} P_c^2}{m_c P} (1 - e_c^2)^{3/2}. \quad (5)$$

The first eccentricity peak is achieved at $t_{\text{KL}}/2$, and the maximum of the eccentricity can be approximated as $\sqrt{1 - (5/3)\cos^2 i_c}$ (Naoz 2016; Nesvold et al. 2016). Assuming that the detected wide companions fulfill the inclination criteria above ($39^\circ \leq i_c \leq 141^\circ$) and are on a circular orbit, and adopting the projected separations as an estimate of the semimajor axes, we can calculate the innermost radius where a third body can undergo the maximum eccentricity phase during the lifetime of system. In the cases of TYC 4209 and TYC 8105, we deduced radii of ~ 140 au and ~ 240 au, respectively. Even the largest known exo-Kuiper belts around solar-type stars have radii < 200 au (Löhne et al. 2012; Faramaz et al. 2019; Sepulveda et al. 2019). Considering this, and that the eccentricities already started increasing inside the above-derived radii, it is conceivable that in TYC 4209, the companion can affect the orbit of planetesimals in an outer belt. A direct entry of a perturbed planetesimal into the sublimation region inside the snow line is possible but would require a high eccentricity (e.g., $e > 0.99$ for a comet originating from a belt at > 100 au), and thus would require a high inclination of the companion ($i_c \gtrsim 84^\circ$ for the previous example). However, even with smaller eccentricities, a planetesimal can cross a chaotic zone of a planet from where it can be transported inward, potentially by multiple scattering in a chain of planets. In BD+20 307, HD 23514, HD 15407, TYC 4479, TYC 4946, and TYC 4515, the eccentricity of a tertiary body can peak within the available time (the age of the system) already at < 1.5 au, ~ 2 au, 4 au, 11 au, < 8 au, and < 15 au, respectively, due to the KL mechanism. It means that in these cases, not only can the outer planetesimal belt be affected, but so too can the possible planetary system within the belt. Changing eccentricities of the planets can lead to a dynamical instability that can enhance the inward transport of comets further (see above). It is also a delayed effect, which can be consistent with the existence of EDDs at > 100 Myr.

In this calculation, for the probable white dwarf companion of BD+20 307, we adopted a mass of $0.48 M_\odot$ (Gentile Fusillo et al. 2019) and a semimajor axis of 980 au. However, the progenitor of this companion was more massive, and the mass loss during the stellar evolution was accompanied by a change in its orbit, making our result on the KL mechanism in this

system uncertain. Further investigation of the white dwarf companion would be important to provide a more accurate age determination (e.g., Founesneau et al. 2019) and to study the dynamical evolution of this interesting triple system. This could lead to a better understanding of the formation of the dusty warm disk as well.

For the semimajor axes of the companions, we adopted the observed projected separations, which are likely smaller than the true semimajor axes. Considering a random distribution of orbital inclinations and the observed eccentricity distribution of binary systems, Fischer & Marcy (1992) found that the true semimajor axes are $1.26\times$ larger on average than the projected separations. Taking into account this multiplicative factor in a statistical manner results in $\sim 1.6\times$ larger inner radii for the area affected by the KL mechanism. This would not change our main conclusions.

Most cometary models assume the presence of an outer, cold planetesimal belt in the system. Based on currently available observations, none of the EDDs with age > 100 Myr show evidence for cold debris belts. Three systems have deep far-IR photometry obtained with the Herschel Space Observatory. For HD 15407 and HD 23514, these observations implied the presence of two temperature components; however, even the colder dust has relatively high temperatures: 334 K and 168 K, respectively (Vican et al. 2016). These temperatures are higher than what is required for sublimation of water ice, and thus they do not indicate regions in which icy planetesimals can persist for a long time. Considering their fractional luminosity, these components, even if they indicated separate rings, could still be of transient origin (Vican et al. 2016). In the case of BD +20 307, the 70 and 100 μm *Herschel* photometries are consistent with the emission of a single warm component. P 1121 harbors no cold dust either (Meng et al. 2015; Su et al. 2019b). As for our six objects, the IRAS FSC catalog provides upper limits at 60 μm for four of them (TYC 4515, TYC 5940, TYC 8105, and TYC 4209). For the other two targets, we used the IRAS SCANPI tool²⁴ to derive upper limits in the same band. On the basis of these IRAS data, even in the best cases, it could only be established that there are no cold (30–80 K) disks with a fractional luminosity greater than 0.01 in our systems. Though there is no direct evidence for colder belts, in most cases, the current data cannot exclude the existence of massive outer debris disks.

It is worth noting that in our previous analyses, we tacitly assumed that only grains for which the ratio of radiation pressure to gravitational force, β , exceeds 0.5 are blown out from the system ($\beta_{\text{bl}} = 0.5$), which is valid if the parent bodies are on a circular orbit. Considering parent bodies on eccentric orbits ($e_{\text{pb}} > 0$), such as comets, β_{bl} can be computed as $\beta_{\text{bl}} = 0.5 \left(\frac{1 - e_{\text{pb}}^2}{1 + e_{\text{pb}} \cos \Phi} \right)$, where Φ is the longitude of the release position on the orbit (Murray & Dermott 1999; Sezestre et al. 2019). This means that depending on the eccentricity, particles with much smaller β parameters (with much larger sizes) can become unbound, and thus the released dust is removed more rapidly than in the circular case. Given typical comet orbits, this obviously requires higher replenishment rates than those obtained from our calculations.

²⁴ <https://irsa.ipac.caltech.edu/applications/Scanpi/>

7. Summary

In this study, we conducted a survey to search for EDDs around sunlike stars. Using the AllWISE IR photometric and the Gaia TGAS astrometric catalogs, and applying careful selection criteria, we found six new EDDs: TYC 4515, TYC 5940, TYC 8105, TYC 4946, TYC 4209, and TYC 4479. Previously, only one of them, TYC 4479, was identified as a debris disk—but not as an EDD—in the literature (Cotten & Song 2016). Host stars of these disks are main-sequence F5–G9 stars located at distances between 164 and 279 pc from the Sun. For their age estimates, we combined different empirical diagnostic methods based on the stars’ lithium content, rotation, and kinematic properties. While the youngest objects have ages similar to that of the Pleiades (~ 120 – 130 Myr), the oldest one, TYC 4479, has an age of ~ 5 Gyr. Actually, the latter system is by far the oldest known EDD. Using astrometric data from Gaia EDR3, we found that five among the six host stars have co-moving pairs with projected separations ranging from 1820 to 6000 au. All of these wide-separation companions are low-mass, M-type stars.

To estimate the basic disk properties, we fitted a simple blackbody model to the observed IR excesses. The dust temperatures are higher than 300 K in all cases, and the derived fractional luminosities range between 0.01 and 0.07. Considering the ages, the observed high amount of warm dust indicates that these systems likely underwent a recent transient event of dust production. Using time-domain photometric data at 3.4 and 4.6 μm from the WISE all-sky surveys between 2010 and 2019, we concluded that the light curves of four systems (TYC 5940, TYC 8105, TYC 4209, and TYC 4479) show evidence of variable mid-IR emission on yearly timescales. We deduced that these variations are associated with the disks and not to the stars. By analyzing the observed 3.4 and 4.6 μm variations, we found that at TYC 4209 and TYC 4479, the observed brightening events seem to be inconsistent with a model where the emitting area of the dust remains constant while its temperature increases. It is more likely that new dust was created temporarily. At TYC 4209, we discovered mid-IR variations at daily timescales as well.

With the six disks studied in this paper, the number of known EDDs increased to 17. Fifteen of them surround sunlike (F5–K2) stars, while two have earlier F-type hosts. Using this new, unified sample, we assessed what they indicate about the nature of these interesting objects. From the 15 sunlike stars, at least nine reside in multiple systems, eight of which are wide-separation binaries with projected separations >365 au. By comparing this incidence with the corresponding statistics for solar-type field stars, we found that very-wide-orbit pairs are significantly more common in EDD systems than in the normal stellar population. The contrast is even stronger if we consider only EDDs older than 100 Myr (10 objects), since all eight wide binary systems belong to this subsample. Based on the literature and on our analysis, 14 of the 17 known EDDs showed changes at 3–5 μm over the past decade. This suggests that the mid-IR variability is an inherent characteristic of EDDs.

The formation of EDDs is generally thought to be linked to giant impacts occurring during the final, chaotic growth phase of terrestrial planets. In our solar system, this phase may have lasted up to ~ 100 million yr. General numerical simulations of rocky planet formation predict that this era could extend up to a

few hundred million years, but the vast majority of giant collisions happen in the first 100 Myr. The observed age distribution of the currently known EDDs is inconsistent with this picture. Only seven of them are younger than 100 Myr, and we know of at least two EDDs that are certainly older than 1 Gyr. If EDDs are indeed linked to rocky planet formation, then these results suggest that the intensity of this process does not decline significantly even after 100 Myr. Alternatively, some other mechanism(s) also produce EDDs. One possible explanation is that the observed dust comes from the disruption and/or collisions of comets delivered from an outer reservoir into the inner regions.

A high fraction of the oldest EDDs—whose existence is most difficult to explain by the classical model—are situated in wide binaries. This raises the possibility that these wide companions may play a role in initiating/maintaining the inward comet transport, e.g., by the KL mechanism, or by launching a comet shower when an eccentric companion approaches an outer population of icy planetesimals. Both invoked mechanisms require time to be activated, and thus could explain the existence of older EDDs. However, further detailed analysis is needed to assess whether these scenarios are able to explain all of the observed features of EDDs.

The authors are grateful to the anonymous referee for the comments, which improved the quality of this manuscript. This publication makes use of data products from the Wide-field Infrared Survey Explorer, which is a joint project of the University of California, Los Angeles, and the Jet Propulsion Laboratory/California Institute of Technology, and NEOWISE, which is a project of the Jet Propulsion Laboratory/California Institute of Technology. WISE and NEOWISE are funded by the National Aeronautics and Space Administration (NASA). This publication makes use of data products from the Two Micron All-Sky Survey, which is a joint project of the University of Massachusetts and the Infrared Processing and Analysis Center/California Institute of Technology, funded by NASA and the National Science Foundation. This work has made use of data from the European Space Agency (ESA) mission Gaia (<https://www.cosmos.esa.int/gaia>), processed by the Gaia Data Processing and Analysis Consortium (DPAC, <https://www.cosmos.esa.int/web/gaia/dpac/consortium>). Funding for DPAC has been provided by national institutions, in particular the institutions participating in the Gaia Multilateral Agreement. This research has made use of the NASA/IPAC Infrared Science Archive, which is operated by the Jet Propulsion Laboratory, California Institute of Technology, under contract with NASA. This research has also made use of the WEBDA database, operated at the Department of Theoretical Physics and Astrophysics of the Masaryk University. We used the VizieR catalog access tool and the Simbad object database at CDS to gather data. Our work is partly based on observations obtained with the Apache Point Observatory 3.5 m telescope, which is owned and operated by the Astrophysical Research Consortium. This project has been supported by the KH130526, K-125015, K-131508, K-119517, and GINOP-2.3.2-15-2016-00003 grants of the National Research, Development and Innovation Office (NKFIH, Hungary) as well as the Lendület Program of the Hungarian Academy of Sciences, project No. LP2018-7/2019. Zs.M.Sz. is supported by the ÚNKP-20-2 New National Excellence Program of the Ministry for Innovation and

Technology from the source of the National Research, Development and Innovation Fund. A.D. was supported by the ÚNKP-20-5 New National Excellence Program of the Ministry for Innovation and Technology from the source of the National Research, Development amid Innovation Fund and the János Bolyai Research Scholarship of the Hungarian Academy of Sciences. A.D. and Gy.M.Sz. would like to thank the City of Szombathely for support under agreement No. 67.177-21/2016. G.C. is supported by NAOJ ALMA Scientific Research grant No. 2019-13B.

Facilities: Akari, IRAS, NEOWISE, Spitzer, TESS, WISE.

Software: mpfit (Markwardt 2009), FITSH (Pál 2012), MUFAN (Kollath 1990).

Appendix A Checking Source Confusion

While the emission is dominated by the stellar photosphere for all of our sources in the W1 band, at longer wavelengths, the contribution of excess increases (Table 4). In the W3 and W4 bands, the measured flux densities exceed the predicted photospheric contributions by at least ~ 4.5 and ~ 8.7 times, respectively. In the case of TYC 4209, the observed excess is dominant even in the W2 band. If the excess is caused by a neighboring source(s), not resolved by WISE, then the position of the emitting source measured in W1 and in the other bands would be different. Another indication would be if the shape of the targets' profile does not match the typical profile of point sources. Examining the shape can also help to detect the effects of possible nearby nebosity.

Since the AllWISE catalog does not include separate positional information for the different bands, we performed our analysis using the original WISE measurements. We utilized the “unWISE” coadds (Lang 2014) of the WISE all-sky survey, which are designed to preserve the intrinsic resolution of the WISE images ($\sim 6''1$, $\sim 6''4$, $\sim 6''5$, and $\sim 12''0$ in the W1, W2, W3, and W4 bands, respectively). This provides a factor of ~ 1.4 narrower PSFs than those of the intentionally blurred “Atlas Image” products of the AllWISE Release. Figure 1 shows the vicinity of the six selected systems in all four WISE bands based on the unWISE data. We fitted 2D Gaussians to the measured brightness profiles of our targets, determining their positions, the mean of the FWHM of the major and minor axes (m_A), and the ratio of the FWHM of the minor to the major axis (r_A). The same parameters were derived using the unWISE data of a comparison sample. For the comparison sample, we kept only those objects from the previously compiled AllWISE list (Section 2) for which the S/N of the flux measurement in each band is greater than the minimum S/N for our six sources. This shortened list was also cross-matched with the TGAS catalog, but this time we did not remove giant stars, and we made no cuts based on the parallax data, resulting in a database with 3732 stars.

For the six EDD candidates, the largest W2 and W3 band offsets compared to the W1 position were $0''062$ and $0''415$. These do not count as outliers because 15% and 6% of the objects in the comparison sample display similar or larger offsets in the W2 and W3 bands, respectively. The W4 images of TYC 4946 and TYC 4479 show some extended nebosity around the sources (in the case of TYC 4479, this can already be noticed to some extent in the W3 image). This may explain that while for the other four objects the W4 offsets remain below $0''7$, for these two targets, we measured offsets of $1''1$.

Nevertheless, even these latter values are consistent with those found for comparison objects with similar W4 band S/N (32% and 27% of them have larger offsets than that of TYC 4946 and TYC 4479, respectively). Neither the size nor the shape of the EDD candidates indicate significant contamination: we found that their m_A and r_A parameters fall within 2.3σ of the comparison sample means in all four bands.

For three targets, additional higher spatial resolution mid-IR data are available. TYC 4479 was serendipitously observed with the IRAC camera on board Spitzer at $3.6\ \mu\text{m}$ and $4.5\ \mu\text{m}$ as part of a larger mapping project (Section 4.2), while TYC 4209 was the target of an extensive IRAC monitoring program at the same wavelengths (A. Moór et al. 2021, in preparation). Our targets appear as single sources in the obtained images that have three times better spatial resolution (FWHM $\sim 2''$) than those of WISE at the corresponding wavelengths. The recently released unWISE Catalog (Schlafly et al. 2019)—which considers all W1 and W2 band images obtained in the WISE and the first 4 yr of the NEOWISE Reactivation missions—lists an object that is located $6''4$ away from TYC 4515. This faint object ($\sim 20\times$ fainter than TYC 4515 in both bands) is actually an M-type companion of TYC 4515 (Section 3.3). However, the observed excess emission surely originates from the primary component. This is justified not only by the WISE observations, but by a $24\ \mu\text{m}$ Spitzer image where the position of the detected source coincides well with the optical position of TYC 4515 (Section 4.2). Thus, based on currently available IR data, we found no sign of confusion or significant contamination at our targets.

Appendix B Analysis of the TESS Data

B.1. Processing of TESS Data

Five of our stars were covered by the TESS spacecraft providing high-quality 30 minute cadence photometric data. Table B1 shows the TESS Input Catalog (TIC) identifiers of our observed targets, as well as the log of their TESS measurements. We started the data reduction with the calibrated full-frame images, which were downloaded from the MAST archive.²⁵ As a first step, following the outline given in Pál et al. (2020), we derived the plate solution using matched sources from the Gaia DR2 catalog. Considering the resemblance of the TESS throughput to that of Gaia G_{RP} (Jordi et al. 2010; Ricker et al. 2015), these matched objects were also utilized to compute a zero-point flux reference based on the G_{RP} magnitudes. By analyzing various TESS full-frame images, we found that the rms of this flux calibration is ~ 0.015 mag. To extract the photometry of our sources, we performed differential image analysis utilizing the `ficonv` and `fiphot` tasks of the FITSH package (Pál 2012). The photometry was performed on 128×128 pixel subframes centered on the targets. The reference frame was constructed by computing a stray light-free median of 11 individual images measured close to the middle of the whole observing sequence. Lastly we identified and removed data points that were affected by momentum wheel desaturation or significant stray light (Pál et al. 2020). If the target was measured in more than one sector, then the above-described procedure was carried out separately in each sector.

²⁵ <https://mast.stsci.edu>

Table B1
TESS Data

Name	TIC ID	Sectors	Time range	P_{rot} (d)	Amplitude (mag)
TYC 4515	TIC 142013492	S19	11/27/2019–12/24/2019	2.455 ^a	0.00026
TYC 5940	TIC 123977701	S6	12/11/2018–01/07/2019	3.756 ^b	0.0083
TYC 8105	TIC 231921033	S5–7	11/15/2018–02/02/2019	5.042 ^c	0.0187
TYC 4209	TIC 233128866	S15–17	08/15/2019–11/02/2019	5.065 ^d	0.0032
		S19–20	11/27/2019–01/21/2020		
		S22–26	02/18/2020–07/04/2020		
TYC 4479	TIC 368374360	S17–18	10/07/2019–11/27/2019	32.08 ^e	0.0012
		S24–25	04/16/2020–06/08/2020		

Notes.

^a There are two additional weaker peaks at $P = 0.585$ and $P = 2.638$ days. ASAS light curve shows no convincing signals.

^b There are weaker Fourier peaks at double/half frequencies. ASAS data show two close peaks ($P = 3.637$ and $P = 3.648$), confirming the findings from TESS observations.

^c Two weaker peaks are found at $P = 5.636$ and $P = 2.509$ days. Some further irregular variations are still present after pre-whitening with these signals. ASAS light curve indicates one signal at $P = 5.003$ days, confirming the TESS analysis.

^d There are additional nearby weak peaks, possibly due to differential rotation, and a signal at double frequency. ASAS light curve confirms the 5 day signal ($P = 5.126$ days).

^e Some weaker Fourier peaks with periods of ≈ 20 days and amplitudes $< 50\%$ that of the main signal are also present.

B.2. Period Analysis

To identify periodic signals in the obtained TESS light curves, we performed a Fourier analysis with the Multi Frequency ANalysis (MUFAN) tool²⁶ developed by Kollath (1990). Using MUFAN, we prepared the discrete Fourier-transformation of the light curve for frequencies 0–10 1/days. We selected the most significant peaks, and after fitting the frequencies, we pre-whitened the light curve, then iterated these steps until no more convincing Fourier peaks were found in the data. In many cases, longer trends (20–30 days) were found in the data. These might have astrophysical background or instrumental trends, but these cannot be confirmed with TESS data only, as their lengths are comparable to the observations themselves.

The TESS data showed periodic or quasiperiodic signals in all cases. In some targets, close to the main Fourier-peak, additional smaller peaks were found: these are generally attributed to differential rotation of the stellar surface, i.e., regions of different latitudes showing slightly different rotational periods. Where available, we also checked light curves from the ASAS database to validate our findings from the TESS data. The derived main periods and amplitudes are summarized in Table B1.

Appendix C

Properties and Long-term Mid-infrared Variability of Previously Known EDDs

Prior to our study, 11 F–K-type stars were reported to host EDDs. In Table C1, we summarize the fundamental properties of these systems.

Using the available single-exposure photometry acquired in the W1 and W2 bands over the different WISE mission phases, we explored the long-term IR variability of the 11 previously known EDDs listed in Table C1. Some of these targets are brighter than 8 and 7 mags in the W1 and W2 bands, respectively, and thus are potentially affected by nonlinearity and saturation effects. As Mainzer et al. (2014) showed for sources brighter than the saturation limits, fluxes measured in

the reactivated NEOWISE mission could be significantly overestimated relative to the AllWISE mission data (see their Figure 6). Therefore, our previously used quality criteria (Section 4.1) were supplemented with an additional one: we ignored those data points where the fraction of the saturated pixels in the profile-fitting area exceeds 0.05 ($w_{\text{lsat}} > 0.05$, $w_{2\text{sat}} > 0.05$). For the three brightest sources, HD 15407, HD 113766, and HD 166191, this criterion removes essentially all data points. In the cases of BD+20 307 and HD 145263, the W1 band data turned out to be heavily saturated, but we could extract the light curve in the W2 band. From the rest of the sample, only the W1 photometry of HD 23514 was somewhat affected by this issue, but it did not prevent the compilation of the light curve. The photometry of ID 8 has a different quality issue: the reduced χ^2 of all of its W1 band profile-fit photometry measurements (w_{lrcchi2}) obtained during the AllWISE mission phase is higher than the critical value we defined (> 5 , Section 4.1). However, looking at the specific observation windows, the standard deviation of the points did not appear to be substantially higher than in the other windows, and therefore we have waived the application of this quality criterion.

In order to assess the long-term variability of the targets, we used the same strategy as described in Section 5.1. For BD +20 307 and HD 145263, we applied only the χ^2 test and found both objects to be constant within the errors of the $4.6 \mu\text{m}$ observations. The mid-IR flux of the disk around TYC 8241-2652-1 dropped significantly before the start of the WISE mission (Melis et al. 2012), and recent observations indicated that the disk has remained depleted (Günther et al. 2017). In the W1/W2 bands, the source does not exhibit significant excess; thus, it is not surprising that we found no variability in either filter. The other five objects (ID 8, P 1121, V488 Per, RZ Psc, and HD 23514), however, proved to be variable at both 3.4 and $4.6 \mu\text{m}$. Apart from HD 23514, significant color (W1 – W2) variations were also detected. Figure C1 displays their average disk flux densities in each observational window, typically separated by ~ 6 months, between 2010 and 2019. To compute these data, we subtracted the photospheric contributions from the measured flux densities. For photospheric models, the stellar parameters were

²⁶ <http://www.konkoly.hu/staff/kollath/mufan.html>

Table C1
Stellar and Disk Properties of Extreme Debris Systems Identified Prior to Our Study

Name	SpT	Dist.	Lum.	T_{eff}	Group	Age	Mult.	T_{BB}	R_{BB}	f_d	Disk Var.	References
(1)	(2)	(pc)	(L_{\odot})	(K)	(6)	(Myr)	(8)	(K)	(au)	(11)	(12)	(13)
RZ Psc	K0IV	184.7	1.0	5350	...	30^{+10}_{-10}	Y	340–500	0.3–0.7	0.049–0.08	Y (W)	9, 17, 21, 35, 37, 38
BD+20 307	F9V	116.9	2.8	6000	...	$\gtrsim 1000$	Y	358–440	0.7–0.9	0.01–0.04	Y (S)	5, 11, 16, 19, 29, 43, 48, 49, 50, 51, 52, 53
HD 15407	F5V	49.3	3.25	6500	ABDor	149^{+51}_{-19}	Y	500–1020	0.13–0.6	0.006–0.0097	Y (S)	3, 26, 29, 32, 49
V488 Per	K3V	172.9	0.3	4900	α Per	85^{+10}_{-10}	Y?	820	0.06	0.16	Y (W)	2, 8, 24, 54, 55
HD 23514	F5V	139.1	3.0	6450	Pleiades	125^{+8}_{-8}	Y	600–1080	0.1–0.4	0.02	Y (S, W)	7, 29, 39, 40, 44, 49
P 1121	F9V	440.4	1.6	6050	NGC 2422	140^{+20}_{-20}	N	460	0.5	0.014–0.020	Y (S, W)	1, 5, 6, 13, 29, 45
ID 8	G6V	355.7	0.7	5500	NGC 2547	35^{+4}_{-4}	N	400	0.4	0.025–0.032	Y (S, W)	14, 18, 28, 30, 31, 45
TYC 8241-2652-1 ^a	K2V	121.3	0.6	4950	LCC	15^{+3}_{-3}	N	450	0.3	0.11	Y (O, W)	15, 27, 34
HD 113766	F2V	108.6	3.9	6800	LCC	15^{+3}_{-3}	Y	490	0.64	0.017	Y (S)	4, 10, 22, 32, 33, 47
HD 145263	F2V	141.2	4.5	6800	US	10^{+3}_{-3}	N	240–290	2.0–2.9	0.01–0.02	N (S, W)	10, 12, 19, 23, 25, 30, 33, 42
HD 166191	G0	100.8	4.0	6000	HD 166191 ^b	10^{+5}_{-5}	N	760	0.3	0.06	Y (S)	20, 32, 36, 41, 46

Notes. Column (1): Name of the star. Column (2): Spectral type. Column (3): Distance (Bailer-Jones et al. 2021). Column (4): Luminosity. Literature data are scaled corresponding to the new distances from Col. 3 when needed. Column (5): Effective temperature. Column (6): Group membership. ABDor: AB Doradus moving group; LCC: Lower Centaurus Crux association; US: Upper Scorpius association. Column (7): Stellar age. In the case of group members, age of the corresponding group is quoted. Column (8): Multiplicity. See Section 6.3.2 for more details. Column (9): Dust temperature or temperature range when several different estimates are available in the literature. In cases where the SED was fitted with two temperature components, the warmer one is considered. Column (10): Disk radius. For comparability with our results presented in Table 1, we quote the blackbody radii that were computed using luminosities and dust temperatures from Col. (4) and Col. (9). For possible caveats related to this approach, see Section 4.3. Column (11): Fractional luminosity. If this is a range, then it shows the scatter of the literature data and is not because of variability. Column (12): Disk variability in the wavelength regime between 3 and 5 μm . Entries in parentheses show what type of measurements were used to examine the variability—S: Spitzer photometry; W: WISE photometry; G: ground-based instruments. Column (13): References: (1) Gaia Collaboration et al. (2018a); (2) Barrado y Navascués et al. (2004); (3) Bell et al. (2015); (4) Chen et al. (2006); (5) Cotten & Song (2016); (6) Cummings & Kalirai (2018); (7) David & Hillenbrand (2015); (8) Deacon & Kraus (2020); (9) de Wit et al. (2013); (10) de Zeeuw et al. (1999); (11) Fekel et al. (2012); (12) Fujiwara et al. (2013); (13) Gorlova et al. (2004); (14) Gorlova et al. (2007); (15) Günther et al. (2017); (16) Hartman & Lépine (2020); (17) Herbig (1960); (18) Jeffries & Oliveira (2005); (19) Kennedy & Wyatt (2013); (20) Kennedy & Wyatt (2014); (21) Kennedy et al. (2020); (22) Lisse et al. (2017); (23) Lisse et al. (2020); (24) Luo et al. (2019); (25) Mannings & Barlow (1998); (26) Melis et al. (2010); (27) Melis et al. (2012); (28) Meng et al. (2014); (29) Meng et al. (2015); (30) Mittal et al. (2015); (31) Olofsson et al. (2012); (32) Oudmaijer et al. (1992); (33) Pecaut et al. (2012); (34) Pecaut & Mamajek (2016); (35) Potravnov et al. (2014); (36) Potravnov et al. (2018); (37) Potravnov et al. (2019); (38) Punzi et al. (2018); (39) Rhee et al. (2008); (40) Rodriguez et al. (2012); (41) Schneider et al. (2013); (42) Smith et al. (2008); (43) Song et al. (2005); (44) Stauffer et al. (1998); (45) Su et al. (2019b); (46) Su et al. (2019a); (47) Su et al. (2020); (48) Thompson et al. (2019); (49) Vican et al. (2016); (50) Weinberger (2008); (51) Weinberger et al. (2011); (52) Whitelock et al. (1991); (53) Zuckerman et al. (2008); (54) Zuckerman et al. (2012); (55) Zuckerman (2015).

^a TYC 8241-2652-1 hosted an unusually dust-rich disk before 2009, whose mid-IR luminosity then decayed significantly over less than 2 yr, leaving behind a colder (<200K), more tenuous disk (Melis et al. 2012). The quoted data show the disk parameters measured before 2009.

^b Kennedy & Wyatt (2014) found that HD 166191 is co-moving with the well-known Herbig Ae star, HD 163296. Later, Potravnov et al. (2018) identified some additional young stars showing similar kinematics that are located close to HD 166191, and they argued that all of these objects belong to a ~ 10 Myr old kinematic group.

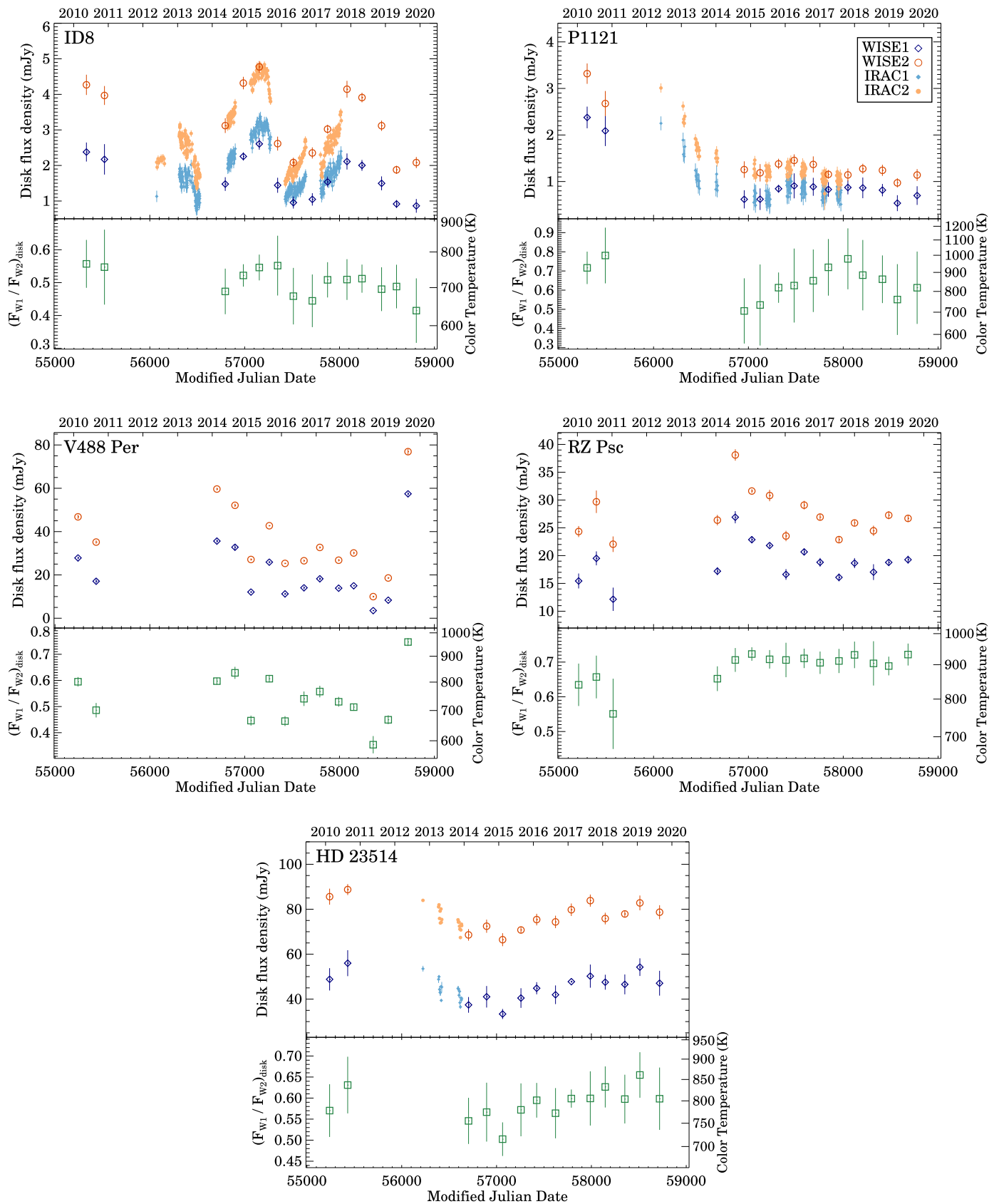





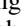



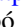



Figure C1. Seasonal averages of W1 and W2 band disk fluxes (top panels) and their ratios (bottom panels) between 2010 and 2019 for five previously known EDDs. Disk fluxes derived from multiyear Spitzer photometric monitoring of HD 23514, ID 8, and P 1121 (Meng et al. 2015; Su et al. 2019b) are also plotted with smaller filled symbols.

taken from the literature, and the corresponding ATLAS9 model was fitted to the available optical and near-IR photometric data of the given source. The bottom panels of each plot show the ratio of W1/W2 disk fluxes and the corresponding color temperatures.

ORCID iDs

Péter Ábrahám  <https://orcid.org/0000-0001-6015-646X>
 Gyula Szabó  <https://orcid.org/0000-0002-0606-7930>
 Krisztián Vida  <https://orcid.org/0000-0002-6471-8607>
 Gianni Cataldi  <https://orcid.org/0000-0002-2700-9676>
 Alíz Derekas  <https://orcid.org/0000-0002-6526-9444>
 Thomas Henning  <https://orcid.org/0000-0002-1493-300X>
 Karen Kinemuchi  <https://orcid.org/0000-0001-7908-7724>
 András Pál  <https://orcid.org/0000-0001-5449-2467>
 Paula Sarkis  <https://orcid.org/0000-0001-8128-3126>
 Bálint Seli  <https://orcid.org/0000-0002-3658-2175>
 Zsófia M. Szabó  <https://orcid.org/0000-0001-9830-3509>

References

- Abbott, T. M. C., Abdalla, F. B., Allam, S., et al. 2018, *ApJS*, 239, 18
 Agüeros, M. A., Bowsher, E. C., Bochanski, J. J., et al. 2018, *ApJ*, 862, 33
 Alam, S., Albareti, F. D., Allende Prieto, C., et al. 2015, *ApJS*, 219, 12
 Almeida-Fernandes, F., & Rocha-Pinto, H. J. 2018, *MNRAS*, 480, 4903
 Amard, L., & Matt, S. P. 2020, *ApJ*, 889, 108
 Andrews, J. J., Chanamé, J., & Agüeros, M. A. 2017, *MNRAS*, 472, 675
 Angus, R., Aigrain, S., Foreman-Mackey, D., & McQuillan, A. 2015, *MNRAS*, 450, 1787
 Bailer-Jones, C. A. L., Rybizki, J., Fouesneau, M., Demleitner, M., & Andrae, R. 2021, *AJ*, 161, 147
 Balachandran, S. 1995, *ApJ*, 446, 203
 Ballering, N. P., Rieke, G. H., Su, K. Y. L., & Gáspár, A. 2017, *ApJ*, 845, 120
 Balog, Z., Kiss, L. L., Vinkó, J., et al. 2009, *ApJ*, 698, 1989
 Baraffe, I., Homeier, D., Allard, F., & Chabrier, G. 2015, *A&A*, 577, A42
 Barclay, T., Quintana, E. V., Raymond, S. N., & Penny, M. T. 2017, *ApJ*, 841, 86
 Barnes, S. A. 2003, *ApJ*, 586, 464
 Barnes, S. A. 2007, *ApJ*, 669, 1167
 Barnes, S. A., Weingrill, J., Fritzewski, D., Strassmeier, K. G., & Platais, I. 2016, *ApJ*, 823, 16
 Barrado y Navascués, D., Stauffer, J. R., & Jayawardhana, R. 2004, *ApJ*, 614, 386
 Beichman, C. A., Lisse, C. M., Tanner, A. M., et al. 2011, *ApJ*, 743, 85
 Bell, C. P. M., Mamajek, E. E., & Naylor, T. 2015, *MNRAS*, 454, 593
 Berski, F., & Dybczyński, P. A. 2016, *A&A*, 595, L10
 Beust, H., Vidal-Madjar, A., & Ferlet, R. 1991, *A&A*, 247, 505
 Blanco-Cuaresma, S., Soubiran, C., Heiter, U., & Jofré, P. 2014, *A&A*, 569, A111
 Boeche, C., & Grebel, E. K. 2016, *A&A*, 587, A2
 Boesgaard, A. M., & Tripicco, M. J. 1986, *ApJL*, 302, L49
 Bonsor, A., Augereau, J. C., & Thébault, P. 2012, *A&A*, 548, A104
 Bonsor, A., Raymond, S. N., & Augereau, J.-C. 2013, *MNRAS*, 433, 2938
 Bonsor, A., Raymond, S. N., Augereau, J.-C., & Ormel, C. W. 2014, *MNRAS*, 441, 2380
 Bonsor, A., & Veras, D. 2015, *MNRAS*, 454, 53
 Booth, M., Wyatt, M. C., Morbidelli, A., Moro-Martín, A., & Levison, H. F. 2009, *MNRAS*, 399, 385
 Bossini, D., Vallenari, A., Bragaglia, A., et al. 2019, *A&A*, 623, A108
 Botke, W. F., & Norman, M. D. 2017, *AREPS*, 45, 619
 Brandeker, A., & Cataldi, G. 2019, *A&A*, 621, A86
 Bressan, A., Marigo, P., Girardi, L., et al. 2012, *MNRAS*, 427, 127
 Burgasser, A. J., Kirkpatrick, J. D., Reid, I. N., et al. 2003, *ApJ*, 586, 512
 Canup, R. M., & Asphaug, E. 2001, *Natur*, 412, 708
 Cardelli, J. A., Clayton, G. C., & Mathis, J. S. 1989, *ApJ*, 345, 245
 Cargile, P. A., James, D. J., & Jeffries, R. D. 2010, *ApJL*, 725, L111
 Carpenter, J. M., Bouwman, J., Mamajek, E. E., et al. 2009, *ApJS*, 181, 197
 Castelli, F., & Kurucz, R. L. 2004, arXiv:astro-ph/0405087
 Chambers, J. E. 2013, *Icar*, 224, 43
 Chambers, K. C., Magnier, E. A., Metcalfe, N., et al. 2016, arXiv:1612.05560
 Chen, C. H., Mittal, T., Kuchner, M., et al. 2014, *ApJS*, 211, 25
 Chen, C. H., Sargent, B. A., Bohac, C., et al. 2006, *ApJS*, 166, 351
 Cotten, T. H., & Song, I. 2016, *ApJS*, 225, 15
 Cruz-Saenz de Miera, F., Chavez, M., Bertone, E., & Vega, O. 2014, *MNRAS*, 437, 391
 Cummings, J. D., & Kalirai, J. S. 2018, *AJ*, 156, 165
 Cutri, R. M., Skrutskie, M. F., van Dyk, S., et al. 2003, *yCat*, 2246
 Cutri, R. M., Wright, E. L., Conrow, T., et al. 2013, *yCat*, II/328
 da Silva, L., Torres, C. A. O., de La Reza, R., et al. 2009, *A&A*, 508, 833
 Dahm, S. E. 2015, *ApJ*, 813, 108
 Daniel, S. A., Latham, D. W., Mathieu, R. D., & Twarog, B. A. 1994, *PASP*, 106, 281
 David, T. J., & Hillenbrand, L. A. 2015, *ApJ*, 804, 146
 Davis, M., Hut, P., & Muller, R. A. 1984, *Natur*, 308, 715
 de Wit, W. J., Grinin, V. P., Potravnov, I. S., et al. 2013, *A&A*, 553, L1
 de Zeeuw, P. T., Hoogerwerf, R., de Bruijne, J. H. J., Brown, A. G. A., & Blaauw, A. 1999, *AJ*, 117, 354
 Deacon, N. R., & Kraus, A. L. 2020, *MNRAS*, 496, 5176
 Dobbie, P. D., Lodieu, N., & Sharp, R. G. 2010, *MNRAS*, 409, 1002
 Douglas, S. T., Curtis, J. L., Agüeros, M. A., et al. 2019, *ApJ*, 879, 100
 Duchêne, G., & Kraus, A. 2013, *ARA&A*, 51, 269
 Elliott, P., Huéramo, N., Bouy, H., et al. 2015, *A&A*, 580, A88
 Ertel, S., Defrère, D., Hinz, P., et al. 2020, *AJ*, 159, 177
 Fabricius, C., Luri, X., Arenou, F., et al. 2020, arXiv:2012.06242
 Faramaz, V., Ertel, S., Booth, M., Cuadra, J., & Simmonds, C. 2017, *MNRAS*, 465, 2352
 Faramaz, V., Krist, J., Stapelfeldt, K. R., et al. 2019, *AJ*, 158, 162
 Fekel, F. C., Cordero, M. J., Galicher, R., et al. 2012, *ApJ*, 749, 7
 Fischer, D. A., & Marcy, G. W. 1992, *ApJ*, 396, 178
 Flaherty, K., Hughes, A. M., Mamajek, E. E., & Murphy, S. J. 2019, *ApJ*, 872, 92
 Fouesneau, M., Rix, H.-W., von Hippel, T., Hogg, D. W., & Tian, H. 2019, *ApJ*, 870, 9
 Frandsen, S., & Lindberg, B. 1999, in *Astrophysics with the NOT*, ed. H. Karttunen & V. Pirola (Piikkio: Univ. Turku), 71
 Fujiwara, H., Ishihara, D., Onaka, T., et al. 2013, *A&A*, 550, A45
 Gagné, J., Mamajek, E. E., Malo, L., et al. 2018, *ApJ*, 856, 23
 Gaia Collaboration, Babusiaux, C., van Leeuwen, F., et al. 2018a, *A&A*, 616, A10
 Gaia Collaboration, Brown, A. G. A., Vallenari, A., et al. 2018b, *A&A*, 616, A1
 Gaia Collaboration, Brown, A. G. A., Vallenari, A., et al. 2020, arXiv:2012.01533
 García, D. E., & Hughes, A. M. 2019, *AAS Meeting*, 233, 163.02
 Geiler, F., & Krivov, A. V. 2017, *MNRAS*, 468, 959
 Genda, H., Kobayashi, H., & Kokubo, E. 2015, *ApJ*, 810, 136
 Gentile Fusillo, N. P., Tremblay, P.-E., Gänsicke, B. T., et al. 2019, *MNRAS*, 482, 4570
 Giampapa, M. S., Hall, J. C., Radick, R. R., & Baliunas, S. L. 2006, *ApJ*, 651, 444
 Gomes, R., Levison, H. F., Tsiganis, K., & Morbidelli, A. 2005, *Natur*, 435, 466
 Gorlova, N., Balog, Z., Rieke, G. H., et al. 2007, *ApJ*, 670, 516
 Gorlova, N., Padgett, D. L., Rieke, G. H., et al. 2004, *ApJS*, 154, 448
 Günther, H. M., Kraus, S., Melis, C., et al. 2017, *A&A*, 598, A82
 Halliday, A. N. 2008, *RSPTA*, 366, 4163
 Hartman, Z. D., & Lépine, S. 2020, *ApJS*, 247, 66
 Helou, G., Khan, I. R., Malek, L., & Boehmer, L. 1988, *ApJS*, 68, 151
 Henden, A. A., Templeton, M., Terrell, D., et al. 2016, *yCat*, 2336
 Herbig, G. H. 1960, *ApJ*, 131, 632
 Høg, E., Fabricius, C., Makarov, V. V., et al. 2000, *A&A*, 357, 367
 Hughes, A. M., Duchêne, G., & Matthews, B. C. 2018, *ARA&A*, 56, 541
 Iglesias, D., Bayo, A., Olofsson, J., et al. 2018, *MNRAS*, 480, 488
 Ishihara, D., Onaka, T., Katata, H., et al. 2010, *A&A*, 514, A1
 Jackson, A. P., & Wyatt, M. C. 2012, *MNRAS*, 425, 657
 Jacobsen, S. B. 2005, *AREPS*, 33, 531
 Jeffries, R. D., & Oliveira, J. M. 2005, *MNRAS*, 358, 13
 Jiang, Y.-F., & Tremaine, S. 2010, *MNRAS*, 401, 977
 Jordi, C., Gebran, M., Carrasco, J. M., et al. 2010, *A&A*, 523, A48
 Juarez, A. J., Cargile, P. A., James, D. J., & Stassun, K. G. 2014, *ApJ*, 795, 143
 Kaib, N. A., Raymond, S. N., & Duncan, M. 2013, *Natur*, 493, 381
 Kaufer, A., Stahl, O., Tubbesing, S., et al. 1999, *Msngr*, 95, 8
 Kawaler, S. D. 1988, *ApJ*, 333, 236
 Kennedy, G. M., Ginski, C., Kenworthy, M. A., et al. 2020, *MNRAS*, 496, L75
 Kennedy, G. M., Kenworthy, M. A., Pepper, J., et al. 2017, *RSOS*, 4, 160652
 Kennedy, G. M., & Piette, A. 2015, *MNRAS*, 449, 2304
 Kennedy, G. M., & Wyatt, M. C. 2013, *MNRAS*, 433, 2334

- Kennedy, G. M., & Wyatt, M. C. 2014, *MNRAS*, **444**, 3164
- Kiefer, F., Lecavelier des Etangs, A., Augereau, J. C., et al. 2014, *A&A*, **561**, L10
- Kleine, T., Touboul, M., Bourdon, B., et al. 2009, *Geochim. Cosmochim. Acta*, **73**, 5150
- Kochanek, C. S., Shappee, B. J., Stanek, K. Z., et al. 2017, *PASP*, **129**, 104502
- Kollath, Z. 1990, Konkoly Observatory Occasional Technical Notes, 1, 1
- Kraft, R. P. 1967, *ApJ*, **150**, 551
- Krivov, A. V. 2010, *RAA*, **10**, 383
- Lada, C. J., Muench, A. A., Rathborne, J., Alves, J. F., & Lombardi, M. 2008, *ApJ*, **672**, 410
- Lang, D. 2014, *AJ*, **147**, 108
- Lindgren, L., Klioner, S. A., Hernández, J., et al. 2020, arXiv:2012.03380
- Lindgren, L., Lammers, U., Bastian, U., et al. 2016, *A&A*, **595**, A4
- Lisse, C. M., Meng, H. Y. A., Sitko, M. L., et al. 2020, *ApJ*, **894**, 116
- Lisse, C. M., Sitko, M. L., Russell, R. W., et al. 2017, *ApJL*, **840**, L20
- Löhne, T., Augereau, J. C., Ertel, S. A. 2008, *ApJ*, **537**, A110
- Luo, A. L., Zhao, Y. H., Zhao, G., et al. 2019, *yCat*, V/164
- Mainzer, A., Bauer, J., Cutri, R. M., et al. 2014, *ApJ*, **792**, 30
- Makovoz, D., & Marleau, F. R. 2005, *PASP*, **117**, 1113
- Mamajek, E. E., & Hillenbrand, L. A. 2008, *ApJ*, **687**, 1264
- Mamajek, E. E., Meyer, M. R., & Liebert, J. 2002, *AJ*, **124**, 1670
- Mann, A. W., Feiden, G. A., Gaidos, E., Boyajian, T., & von Braun, K. 2015, *ApJ*, **804**, 64
- Mannings, V., & Barlow, M. J. 1998, *ApJ*, **497**, 330
- Marboeuf, U., Bonsor, A., & Augereau, J. C. 2016, *P&SS*, **133**, 47
- Marino, S., Bonsor, A., Wyatt, M. C., & Kral, Q. 2018, *MNRAS*, **479**, 1651
- Marino, S., Wyatt, M. C., Panić, O., et al. 2017, *MNRAS*, **465**, 2595
- Markwardt, C. B. 2009, in *ASP Conf. Ser.* 411, *Astronomical Data Analysis Software and Systems XVIII*, ed. D. A. Bohlender, D. Durand, & P. Dowler (San Francisco, CA: ASP), 251
- Meibom, S., Mathieu, R. D., & Stassun, K. G. 2009, *ApJ*, **695**, 679
- Melis, C., Zuckerman, B., Rhee, J. H., et al. 2012, *Natur*, **487**, 74
- Melis, C., Zuckerman, B., Rhee, J. H., & Song, I. 2010, *ApJL*, **717**, L57
- Meng, H. Y. A., Rieke, G. H., Su, K. Y. L., et al. 2012, *ApJL*, **751**, L17
- Meng, H. Y. A., Su, K. Y. L., Rieke, G. H., et al. 2014, *Sci*, **345**, 1032
- Meng, H. Y. A., Su, K. Y. L., Rieke, G. H., et al. 2015, *ApJ*, **805**, 77
- Michalik, D., Lindgren, L., & Hobbs, D. 2015, *A&A*, **574**, A115
- Mittal, T., Chen, C. H., Jang-Condell, H., et al. 2015, *ApJ*, **798**, 87
- Montesinos, B., Eiroa, C., Krivov, A. V., et al. 2016, *A&A*, **593**, A51
- Morales, F. Y., Rieke, G. H., Werner, M. W., et al. 2011, *ApJL*, **730**, L29
- Moshir, M., Kopan, G., Conrow, T., et al. 1990, *BAAS*, **22**, 1325
- Murray, C. D., & Dermott, S. F. 1999, *Solar System Dynamics* (Cambridge: Cambridge Univ. Press)
- Naoz, S. 2016, *ARA&A*, **54**, 441
- Nesvold, E. R., Naoz, S., Vican, L., & Farr, W. M. 2016, *ApJ*, **826**, 19
- Nesvorný, D., Jenniskens, P., Levison, H. F., et al. 2010, *ApJ*, **713**, 816
- Neugebauer, G., Habing, H. J., van Duinen, R., et al. 1984, *ApJL*, **278**, L1
- Olofsson, J., Juhász, A., Henning, T., et al. 2012, *A&A*, **542**, A90
- Oudmajer, R. D., van der Veen, W. E. C. J., Waters, L. B. F. M., et al. 1992, *A&AS*, **96**, 625
- Pál, A. 2012, *MNRAS*, **421**, 1825
- Pál, A., Szakáts, R., Kiss, C., et al. 2020, *ApJS*, **247**, 26
- Pascucci, I., Testi, L., Herczeg, G. J., et al. 2016, *ApJ*, **831**, 125
- Patel, R. I., Metchev, S. A., & Heinze, A. 2014, *ApJS*, **212**, 10
- Patel, R. I., Metchev, S. A., Heinze, A., & Trollo, J. 2017, *AJ*, **153**, 54
- Pawellek, N., Krivov, A. V., Marshall, J. P., et al. 2014, *ApJ*, **792**, 65
- Pecaut, M. J., & Mamajek, E. E. 2013, *ApJS*, **208**, 9
- Pecaut, M. J., & Mamajek, E. E. 2016, *MNRAS*, **461**, 794
- Pecaut, M. J., Mamajek, E. E., & Bubar, E. J. 2012, *ApJ*, **746**, 154
- Pilbratt, G. L., Riedinger, J. R., Passvogel, T., et al. 2010, *A&A*, **518**, L1
- Potravnov, I. S., Eiselevich, M. V., Kondratieva, T. E., & Sokolov, I. V. 2018, *AsTL*, **44**, 603
- Potravnov, I. S., Grinin, V. P., Ilyin, I. V., & Shakhovskoy, D. N. 2014, *A&A*, **563**, A139
- Potravnov, I. S., Grinin, V. P., & Serebriakova, N. A. 2019, *A&A*, **630**, A64
- Potravnov, I. S., Mkrtychian, D. E., Grinin, V. P., Ilyin, I. V., & Shakhovskoy, D. N. 2017, *A&A*, **599**, A60
- Punzi, K. M., Kastner, J. H., Melis, C., et al. 2018, *AJ*, **155**, 33
- Qian, S.-B., Shi, X.-D., Zhu, L.-Y., et al. 2019, *RAA*, **19**, 064
- Quintana, E. V., Barclay, T., Borucki, W. J., Rowe, J. F., & Chambers, J. E. 2016, *ApJ*, **821**, 126
- Raghavan, D., McAlister, H. A., Henry, T. J., et al. 2010, *ApJS*, **190**, 1
- Rebollido, I., Eiroa, C., Montesinos, B., et al. 2020, *A&A*, **639**, A11
- Rebull, L. M., Stauffer, J. R., Bouvier, J., et al. 2016, *AJ*, **152**, 113
- Reidemeister, M., Krivov, A. V., Stark, C. C., et al. 2011, *A&A*, **527**, A57
- Rhee, J. H., Song, I., & Zuckerman, B. 2008, *ApJ*, **675**, 777
- Rhee, J. H., Song, I., Zuckerman, B., & McElwain, M. 2007, *ApJ*, **660**, 1556
- Ricker, G. R., Winn, J. N., Vanderspek, R., et al. 2015, *JATIS*, **1**, 014003
- Rieke, G. H., Young, E. T., Engelbracht, C. W., et al. 2004, *ApJS*, **154**, 25
- Riello, M., De Angeli, F., Evans, D. W., et al. 2020, arXiv:2012.01916
- Rigley, J. K., & Wyatt, M. C. 2020, *MNRAS*, **497**, 1143
- Rodriguez, D. R., Marois, C., Zuckerman, B., Macintosh, B., & Melis, C. 2012, *ApJ*, **748**, 30
- Rowan-Robinson, M., & May, B. 2013, *MNRAS*, **429**, 2894
- Sarajedini, A., Dotter, A., & Kirkpatrick, A. 2009, *ApJ*, **698**, 1872
- Schatzman, E. 1962, *AnAp*, **25**, 18
- Schlafly, E. F., Meisner, A. M., & Green, G. M. 2019, *ApJS*, **240**, 30
- Schneider, A., Song, I., Melis, C., et al. 2013, *ApJ*, **777**, 78
- Sestrec, N. J., & Satyapal, S. 2020, *ApJ*, **900**, 56
- Sepulveda, A. G., Matrà, L., Kennedy, G. M., et al. 2019, *ApJ*, **881**, 84
- Sestito, P., & Randich, S. 2005, *A&A*, **442**, 615
- Sezestre, É., Augereau, J. C., & Thébault, P. 2019, *A&A*, **626**, A2
- Shappee, B. J., Prieto, J. L., Grupe, D., et al. 2014, *ApJ*, **788**, 48
- Sibthorpe, B., Kennedy, G. M., Wyatt, M. C., et al. 2018, *MNRAS*, **475**, 3046
- Silverberg, S. M., Wisniewski, J. P., Kuchner, M. J., et al. 2020, *ApJ*, **890**, 106
- Silverstone, M. D., Meyer, M. R., Mamajek, E. E., et al. 2006, *ApJ*, **639**, 1138
- Skrutskie, M. F., Cutri, R. M., Stiening, R., et al. 2006, *AJ*, **131**, 1163
- Smith, R., Wyatt, M. C., & Dent, W. R. F. 2008, *A&A*, **485**, 897
- Snedden, C. A. 1973, PhD thesis, The University of Texas at Austin
- Soderblom, D. R., Jones, B. F., Balachandran, S., et al. 1993, *AJ*, **106**, 1059
- Sokolovsky, K. V., Gavras, P., Karampelas, A., et al. 2017, *MNRAS*, **464**, 274
- Song, I., Zuckerman, B., Weinberger, A. J., & Becklin, E. E. 2005, *Natur*, **436**, 363
- Soubiran, C., Cantat-Gaudin, T., Romero-Gómez, M., et al. 2018, *A&A*, **619**, A155
- Stauffer, J., Rebull, L., Bouvier, J., et al. 2016, *AJ*, **152**, 115
- Stauffer, J. R., Schultz, G., & Kirkpatrick, J. D. 1998, *ApJL*, **499**, L199
- Steinhauer, A., & Deliyannis, C. P. 2004, *ApJL*, **614**, L65
- Stetson, P. B. 1996, *PASP*, **108**, 851
- Su, K., Rieke, G., & Sand, D. 2019a, *ATel*, **12986**, 1
- Su, K. Y. L., Jackson, A. P., Gáspár, A., et al. 2019b, *AJ*, **157**, 202
- Su, K. Y. L., Rieke, G. H., Melis, C., et al. 2020, *ApJ*, **898**, 21
- Su, K. Y. L., Rieke, G. H., Stansberry, J. A., et al. 2006, *ApJ*, **653**, 675
- Telting, J. H., Avila, G., Buchhave, L., et al. 2014, *AN*, **335**, 41
- Tera, F., Papanastassiou, D. A., & Wasserburg, G. J. 1974, *E&PSL*, **22**, 1
- Thompson, M. A., Weinberger, A. J., Keller, L. D., Arnold, J. A., & Stark, C. C. 2019, *ApJ*, **875**, 45
- Thureau, N. D., Greaves, J. S., Matthews, B. C., et al. 2014, *MNRAS*, **445**, 2558
- Tokovinin, A., & Briceño, C. 2020, *AJ*, **159**, 15
- Tonry, J. L., Stubbs, C. W., Lykke, K. R., et al. 2012, *ApJ*, **750**, 99
- Touboul, M., Kleine, T., Bourdon, B., Palme, H., & Wieler, R. 2007, *Natur*, **450**, 1206
- Twarog, B. A., Anthony-Twarog, B. J., Deliyannis, C. P., & Thomas, D. T. 2015, *AJ*, **150**, 134
- VandenBerg, D. A., & Stetson, P. B. 2004, *PASP*, **116**, 997
- Vican, L., Schneider, A., Bryden, G., et al. 2016, *ApJ*, **833**, 263
- Villanova, S., Carraro, G., & Saviane, I. 2009, *A&A*, **504**, 845
- Weinberg, M. D., Shapiro, S. L., & Wasserman, I. 1987, *ApJ*, **312**, 367
- Weinberger, A. J. 2008, *ApJL*, **679**, L41
- Weinberger, A. J., Becklin, E. E., Song, I., & Zuckerman, B. 2011, *ApJ*, **726**, 72
- Welsh, B. Y., & Montgomery, S. L. 2015, *AdAst*, **2015**, 980323
- Werner, M. W., Roellig, T. L., Low, F. J., et al. 2004, *ApJS*, **154**, 1
- Whitelock, P. A., Menzies, J. W., Catchpole, R. M., et al. 1991, *MNRAS*, **250**, 638
- Wright, E. L., Eisenhardt, P. R. M., Mainzer, A. K., et al. 2010, *AJ*, **140**, 1868
- Wyatt, M. C. 2008, *ARA&A*, **46**, 339
- Wyatt, M. C., Smith, R., Greaves, J. S., et al. 2007, *ApJ*, **658**, 569
- Zuckerman, B. 2015, *ApJ*, **798**, 86
- Zuckerman, B., Fekel, F. C., Williamson, M. H., Henry, G. W., & Muno, M. P. 2008, *ApJ*, **688**, 1345
- Zuckerman, B., Klein, B., & Kastner, J. 2019, *ApJ*, **887**, 87
- Zuckerman, B., Melis, C., Rhee, J. H., Schneider, A., & Song, I. 2012, *ApJ*, **752**, 58